



OPEN

# Ras-mutant cancers are sensitive to small molecule inhibition of V-type ATPases in mice

Bhairavi Tolani<sup>1</sup>✉, Anna Celli<sup>2</sup>, Yanmin Yao<sup>3</sup>, Yong Zi Tan<sup>4,16,17</sup>, Richard Fetter<sup>5</sup>, Christina R. Liem<sup>6,18</sup>, Adam J. de Smith<sup>7</sup>, Thamiya Vasanthakumar<sup>4,8</sup>, Paola Bisignano<sup>3</sup>, Adam D. Cotton<sup>3</sup>, Ian B. Seiple<sup>3</sup>, John L. Rubinstein<sup>4,8,9</sup>, Marco Jost<sup>6,10,11</sup>✉ and Jonathan S. Weissman<sup>6,12,13,14,15</sup>

**Mutations in Ras family proteins are implicated in 33% of human cancers, but direct pharmacological inhibition of Ras mutants remains challenging. As an alternative to direct inhibition, we screened for sensitivities in Ras-mutant cells and discovered 249C as a Ras-mutant selective cytotoxic agent with nanomolar potency against a spectrum of Ras-mutant cancers. 249C binds to vacuolar (V)-ATPase with nanomolar affinity and inhibits its activity, preventing lysosomal acidification and inhibiting autophagy and macropinocytosis pathways that several Ras-driven cancers rely on for survival. Unexpectedly, potency of 249C varies with the identity of the Ras driver mutation, with the highest potency for KRASG13D and G12V both in vitro and in vivo, highlighting a mutant-specific dependence on macropinocytosis and lysosomal pH. Indeed, 249C potently inhibits tumor growth without adverse side effects in mouse xenografts of KRAS-driven lung and colon cancers. A comparison of isogenic SW48 xenografts with different KRAS mutations confirmed that KRASG13D/+ (followed by G12V/+) mutations are especially sensitive to 249C treatment. These data establish proof-of-concept for targeting V-ATPase in cancers driven by specific KRAS mutations such as KRASG13D and G12V.**

Mutations that constitutively activate members of the Ras family of oncogenes (H-Ras, N-Ras, and K-Ras) are collectively responsible for about one third of all human cancers; KRAS mutations in particular are implicated in the most fatal malignancies: pancreatic (91%), colon (42%) and lung (33%)<sup>1–4</sup>. Despite decades-long efforts, we still lack clinically-approved drugs for the majority of oncogenic KRAS variants (apart from Amgen's KRASG12C inhibitor), in large part because of substantial challenges in directly inhibiting mutant KRAS. As an alternative strategy for pharmacological intervention, efforts to map potentially druggable neomorphic dependencies of KRAS-mutant cancers have identified, among others, metabolic adaptations concomitant with activating KRAS mutations, including high levels of basal autophagy, a phenomenon termed 'autophagy addiction'<sup>5–9</sup>, and constitutive activation of macropinocytosis (MP)<sup>10</sup>. Both autophagy and MP provide nutrients to promote tumor growth by degrading macromolecules in acidic lysosomes produced by vacuolar H<sup>+</sup> ATPases (V-ATPases)<sup>11,12</sup>, and V-ATPase has been reported as an essential regulator of Ras-induced MP for nutrient supply, suggesting that targeting V-ATPase could be exploited to curtail the metabolic adaptation of Ras-mutant cells<sup>10</sup>.

V-ATPase is a multi-subunit transmembrane complex that operates as an ATP-driven rotary proton pump, coupling ATP hydrolysis in its peripheral V<sub>1</sub> domain to proton translocation from the cytoplasm to the lumen of organelles through its membrane integral V<sub>o</sub> domain. Through this activity, V-ATPase is essential for lysosome acidification and thus lysosomal degradation<sup>13,14</sup> and more broadly regulates a wide array of membrane trafficking and intracellular transport processes<sup>15</sup>. Although specific V-ATPase inhibitors such as Bafilomycin A1 (BafA1) have been developed and serve as important tool compounds, their clinical use is limited by toxicity<sup>16</sup>. Additional autophagy-modulating agents have been described, such as the repurposed antimalarial compound chloroquine (CQ) and its less toxic derivative hydroxychloroquine (HCQ), which impair lysosomal acidification by targeting palmitoyl-protein thioesterase 1 (PPT1), but these compounds have severe side effects by interfering with human ether-à-go-go-related gene (hERG) responsible for electrical activity of the heart<sup>17,18</sup> and they can also cause gastrointestinal side effects, impact visual and auditory function, and lead to hypoglycemia. In over 60 clinical trials (completed or ongoing), CQ or HCQ alone as a monotherapy do not demonstrate substantial therapeutic efficacy<sup>19</sup>. Although second-generation analogs of

<sup>1</sup>Thoracic Oncology Program, Department of Surgery, Helen Diller Family Comprehensive Cancer Center, University of California, San Francisco, CA, USA. <sup>2</sup>Laboratory for Cell Analysis Core Facility, Helen Diller Family Comprehensive Cancer Center, University of California, San Francisco, CA, USA.

<sup>3</sup>Department of Pharmaceutical Chemistry and Cardiovascular Research Institute, University of California, San Francisco, CA, USA. <sup>4</sup>Molecular Medicine Program, The Hospital for Sick Children, Toronto, ON, Canada. <sup>5</sup>Howard Hughes Medical Institute, Department of Biology, Stanford University, Stanford, CA, USA. <sup>6</sup>Department of Cellular and Molecular Pharmacology, University of California, San Francisco, San Francisco, CA, USA. <sup>7</sup>Center for Genetic Epidemiology, Department of Population and Public Health Sciences, Keck School of Medicine of University of Southern California, Los Angeles, CA, USA.

<sup>8</sup>Department of Biochemistry, The University of Toronto, Toronto, ON, Canada. <sup>9</sup>Department of Medical Biophysics, The University of Toronto, Toronto, ON, Canada. <sup>10</sup>Department of Microbiology & Immunology, University of California, San Francisco, CA, USA. <sup>11</sup>Department of Microbiology, Harvard Medical School, Boston, MA, USA. <sup>12</sup>Howard Hughes Medical Institute, Massachusetts Institute of Technology, Cambridge, MA, USA. <sup>13</sup>Whitehead Institute for Biomedical Research, Massachusetts Institute of Technology, Cambridge, MA, USA. <sup>14</sup>David H. Koch Institute for Integrative Cancer Research, Massachusetts Institute of Technology, Cambridge, MA, USA. <sup>15</sup>Department of Biology, Massachusetts Institute of Technology, Cambridge, MA, USA.

<sup>16</sup>Present address: Department of Biological Sciences, National University of Singapore, Singapore, Singapore. <sup>17</sup>Present address: Disease Intervention Technology Laboratory, Agency for Science, Technology and Research, Singapore, Singapore. <sup>18</sup>Present address: Division of Biological Sciences, the Section of Cell and Developmental Biology, University of California San Diego, La Jolla, CA, USA. ✉e-mail: [Bhairavi.Tolani@ucsf.edu](mailto:Bhairavi.Tolani@ucsf.edu); [marco.jost@hms.harvard.edu](mailto:marco.jost@hms.harvard.edu)

HCQ such as ROC325, Lys05, DC661, and DQ661 show enhanced preclinical lysosomal-autophagic inhibition and antitumor activity as single agents *in vitro* and *in vivo*, it remains to be determined whether any of them will show efficacy in clinical investigations while avoiding unacceptable toxicities<sup>17,20</sup>. These limitations motivate an urgent need to identify and develop additional autophagy/MP inhibitors with clean safety profiles.

Here we report the discovery and characterization of a class of dihydro-pyrazole-5-carboxamide compounds with exquisite potency in killing *KRAS*-mutant cells and excellent pharmacological properties. By combining chemoproteomics, comparative profiling, and chemo-genetic clustered regularly interspaced short palindromic repeats (CRISPR) screening, we determined that our lead compound 249C binds to and inhibits V-ATPase, resulting in inhibition of autophagy, MP, and lysosomal acidification. Through this activity, 249C selectively kills *KRAS/BRAF*-mutant cells, with the highest activity against *KRASG13D* and *G12V* mutant cells, pointing to excessive reliance on V-ATPase as a unique vulnerability resulting from these *KRAS* mutations. For over 1 year, the molecule has been in a multi-center Phase Ia/b dose escalation and dose expansion clinical trial for the following indications: Ras mutations, lung, colon, and pancreatic cancers across five different sites in the U.S. (NCT04678648; 249C = RSC-1255).

## Results

**249C is a potent inhibitor of Ras- and Raf-mutant cells.** We had recently synthesized ~300 dihydro-pyrazole-5-carboxamide small molecules to target a developmental pathway (Supplementary Fig. 1 and Supplementary Table 1). Here to evaluate the ability of these molecules to also inhibit growth of Ras- and Raf-mutant cells, we screened these molecules for anti-proliferative activity against three human cancer cell lines with mutations in Ras or Raf: A549 (*KRASG12S*); LOX IMVI (*BRAFV600E*); and MelJuso (*HRASG13D* and *NRASQ61L*). Using structure-activity relationships, we observed that several compounds potentially reduced viability of all three cell lines (Fig. 1a and Supplementary Tables 1–3). Simultaneous evaluation of drug-like properties and half-maximal inhibitory concentration ( $IC_{50}$ ) values revealed 249C as the lead compound on the basis of physico-chemical properties (Fig. 1b,c). Compound 249C was chosen over 226C for further studies owing to the presence of a tertiary amine, imparting higher water solubility, and a slightly lower  $cLogP$  (3.07 versus 3.33). To further evaluate determinants of sensitivity to 249C, we measured its potency against 53 cell lines (lung, pancreatic, breast, ovarian, colorectal/gastric, prostate, liver/hematological, glioma, and melanoma) (Fig. 1d). Comparing  $IC_{50}$  values to gene mutation data from the Cancer Cell Line Encyclopedia (CCLE) revealed that the presence of at least one mutation in *KRAS*, *HRAS*, *NRAS*, and/or *BRAF* was significantly associated with lower  $IC_{50}$  values ( $P = 1.24 \times 10^{-6}$ ), with median  $IC_{50}$  values of 65 nM in *KRAS/HRAS/NRAS/BRAF*-mutant cells versus 365 nM in cells with no mutations in these genes (Fig. 1e). *KRAS* showed the strongest single gene association with  $IC_{50}$  values ( $P = 2.34 \times 10^{-3}$ ) (Supplementary Fig. 1b,c). We next mapped the response of A549 cells to these compounds using liquid chromatography–tandem mass spectrometry (LC–MS/MS)-based protein profiling coupled with quantitative tandem mass tags labeling<sup>21</sup>. Upon treatment of cells with vehicle or molecules 68, 226C and 249C, we observed substantially elevated levels of the autophagy receptor sequestosome 1 (SQSTM1/p62) common to this family of compounds (Fig. 1f) in a time-dependent fashion (Fig. 1g), suggesting that these compounds impact autophagy.

**249C inhibits autophagy.** To characterize the mode of action of our lead compound 249C, we used comparative profiling in a panel of primary-cell-based systems designed to model disease biology<sup>22</sup>. In comparison to 4,000 other drugs, the phenotypes elicited by 249C

most closely resembled those elicited by the V-ATPase inhibitor BafA1 (Pearson's  $r = 0.95$  across all measurements; Fig. 2a,b, Supplementary Figs. 2 and 3, and Supplementary Table 4). 249C also exhibited similarity, albeit to a lesser degree, to the mTOR inhibitors rapamycin and Torin1 and the antimalarials CQ and quinacrine. 249C and BafA1 elicited progressive accumulation of SQSTM1/p62 and microtubule-associated protein 1A/1B-light chain 3 (LC3-II) in A549 cells, consistent with a block in autophagic flux; by contrast, the autophagy inducer rapamycin did not (Fig. 2c). Using transmission electron microscopy, we further observed late-stage autophagy inhibition and increased autophagic vesicle accumulation in A549 cells treated with 249C and BafA1 (Fig. 2d–i). Finally, treatment with both 249C and BafA1 caused a reduction in the presence of acidic organelles (Fig. 2j) and an increase in pH (Fig. 2j) of A549 cells relative to dimethyl sulfoxide (DMSO) and Torin1, confirming that 249C blocks lysosomal acidification and autophagy progression.

**Chemical-genetic screen reveals V-ATPase as the target of 249C.** To further pinpoint the molecular target of 249C, we turned to CRISPR interference (CRISPRi)-mediated chemical-genetic screening, which has emerged as a robust strategy for identification of small molecule targets<sup>23</sup>. To allow us to work with a previously validated CRISPRi cell line, we evaluated a panel of available CRISPRi cell lines for sensitivity to 249C and found that MDA-MB-231 cells (breast adenocarcinoma, *KRASG13D* and *BRAFV600E*) were highly sensitive. Thus, we conducted these screens in MDA-MB-231 cells. In brief, we infected MDA-MB-231 cells stably expressing the dCas9-KRAB CRISPRi effector<sup>24</sup> with the genome-scale hCRISPRi-v2 single-guide RNA (sgRNA) library (targeting 18,905 genes)<sup>25</sup>, harvested a subpopulation at the outset of the experiment ( $t_0$ ), and then cultured the remaining cells without (DMSO) or with 249C treatment (Methods). Finally, we used next-generation sequencing to determine how each sgRNA impacted sensitivity to 249C ( $\rho$ ) and growth in the absence of 249C ( $\gamma$ )<sup>26</sup> (Fig. 3a). The resulting untreated growth phenotypes were well correlated with those from other cell types, suggesting that our screen faithfully captured phenotypes resulting from gene knockdown (Supplementary Fig. 4). Among the 147 genes for which knockdown strongly affected 249C sensitivity (Fig. 3b and Supplementary Tables 5 and 6), we were intrigued to find five V-ATPase subunits (*ATP6VIH*, *ATP6V1A*, *ATP6VoA2*, *ATP6VoA3/TCIRG1*, and *ATP6VoE1*), because 249C essentially phenocopied the V-ATPase inhibitor BafA1 in our previous assays (Fig. 2c). Indeed, knockdown of several V-ATPase subunits sensitized cells to 249C; the regulatory H subunit *ATP6VIH* in particular was one of the most strongly sensitizing hits. By contrast, knockdown of the poorly characterized subunits *ATP6VoE1* and *ATP6VoA3/TCIRG1* protected cells against 249C. Individual re-tests using internally controlled drug-sensitivity assays further confirmed that knockdown of multiple V-ATPase subunits sensitized MDA-MB-231 cells to 249C and BafA1 (target: *ATP6VoC*)<sup>27</sup> (Fig. 3c). Thus, genetic depletion of V-ATPase sensitizes cells to 249C, further suggesting that the cytotoxicity of 249C arises from inhibition of V-ATPase activity. Although we cannot rule out polypharmacology, the V-ATPase complex stood out on the basis of multiple subunit hits.

**249C binds and inhibits V-ATPase.** With multiple independent assays pointing toward V-ATPase as the target of 249C, we proceeded to validate the biochemical and biophysical effects of 249C on V-ATPase activity. V-ATPase activity depends upon reversible assembly of the  $V_1$  and  $V_0$  domains and is nutrient dependent; increased  $V_1$ - $V_0$  assembly increases catalytic activity<sup>15</sup>. To test whether 249C alters localization of V-ATPase subunits, we evaluated the partitioning of V-ATPase subunits into the cytosolic (containing the  $V_1$  domain composed of eight subunits (A–H) responsible for

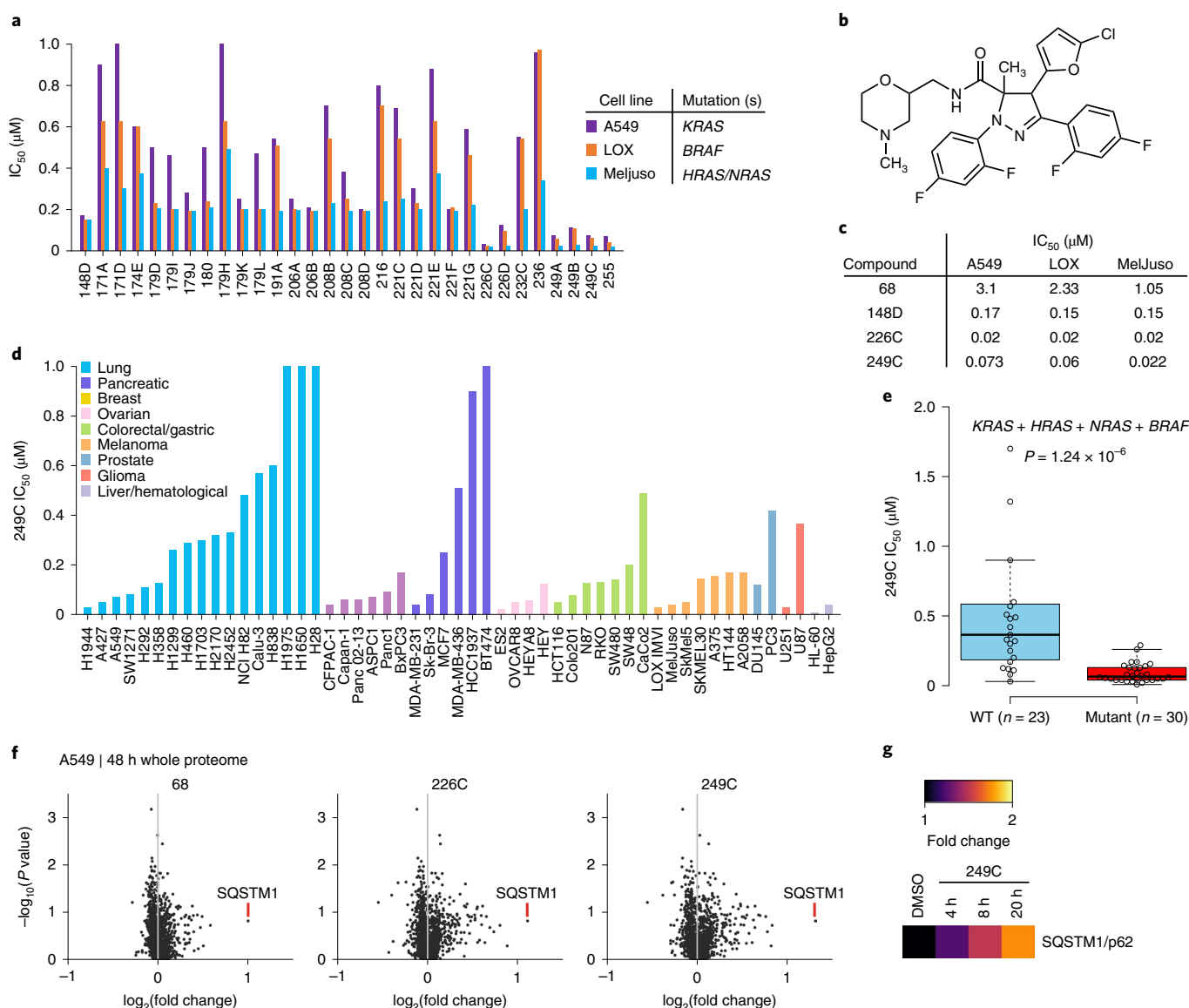


**Fig. 1 | Optimization of potency and drug properties of small molecule inhibitors of Ras- and Raf-mutant cells using viability screens. a**, Cell viability screen of ~300 small molecules in A549 (*KRAS*G12S), LOX IMV1 (*BRAF*V600E), and MelJuso (*HRAS*G13D and *NRAS*Q61L). Cells were treated with vehicle DMSO or increasing concentrations of small molecules in triplicate for 72 h and ATP content/viability was measured using CellTiter-Glo Luminescent Cell Viability Assay. The results shown for all cell viability figures are representative of at least two independent experiments. The top 30 compounds ( $P < 0.05$  in comparison to vehicle-treated controls, two-sided *t*-test) with the lowest IC<sub>50</sub>s are presented.  $n = 3$ . **b**, Structure of dihydro-pyrazole-5-carboxamide small molecule hit 249C that shows inhibition of viability in both Ras- and Raf-mutant cells. **c**, Evolution of the structure-activity relationship and IC<sub>50</sub> of the first (68) and last (249C; lead owing to drug-like properties) compounds in the screen. **d**, 249C sensitivity for a panel of 53 cancer cell lines (including lung, pancreatic, breast, ovarian, hematological/liver, prostate, colorectal cancers, glioma, and melanoma). **e**, IC<sub>50</sub> values stratified by the mutation status of *KRAS*, *HRAS*, *NRAS*, and *BRAF* (two-sided Wilcoxon rank sum test;  $P = 1.24 \times 10^{-6}$ ; Supplementary Fig. 1). The center line represents the median, the upper and lower bounds of the box indicate the interquartile range (IQR, the range between the 25th and 75th percentiles), and whiskers extend to the highest and lowest values within 1.5 times the IQR. **f**, Quantitative whole proteome analysis of the effects of small molecule treatment by mass spectrometry. A549 cells were treated with DMSO or 68 (30 µM), 226C (1 µM) or 249C (1 µM) for 48 h before analysis of proteomes with TMT labeling followed by quantification relative to the DMSO control. Autophagy receptor, SQSTM1, was identified as highly upregulated and common for our family of compounds by proteomic mass spectrometric screening in small molecule-treated A549 mutant *KRAS* cells. More data can be found in Supplementary Fig. 2 and Supplementary Tables 1–3. **g**, Quantitative whole proteome analysis of 249C-treated (1 µM) A549 cells over time relative to DMSO control.

ATP hydrolysis) and membrane fractions (membrane-embedded Vo domain comprised of six subunits (a, c, c' (absent in mammals), c'', d and e) responsible for proton translocation)<sup>15</sup> of 249C-treated HEK293T cells. Treatment with 249C but not BafA1 led to an increase in membrane-associated subunit B2 (cytosolic V<sub>1</sub> domain), possibly indicating increased V-ATPase assembly (Fig. 4a,b). To independently corroborate the effect of 249C on

V-ATPase and to probe whether proton pumping is impacted in the complexes on lysosomes, we measured lysosome acidification using a pH-dependent fluorescent probe, FITC-Dextran. Both 249C and BafA1 inhibited V-ATPase-dependent proton transport in mammalian cells, as measured by ATP-dependent fluorescence quenching of FITC-loaded lysosomes<sup>28</sup> (Fig. 3c). Proton translocation through the Vo region is powered by ATP hydrolysis in the

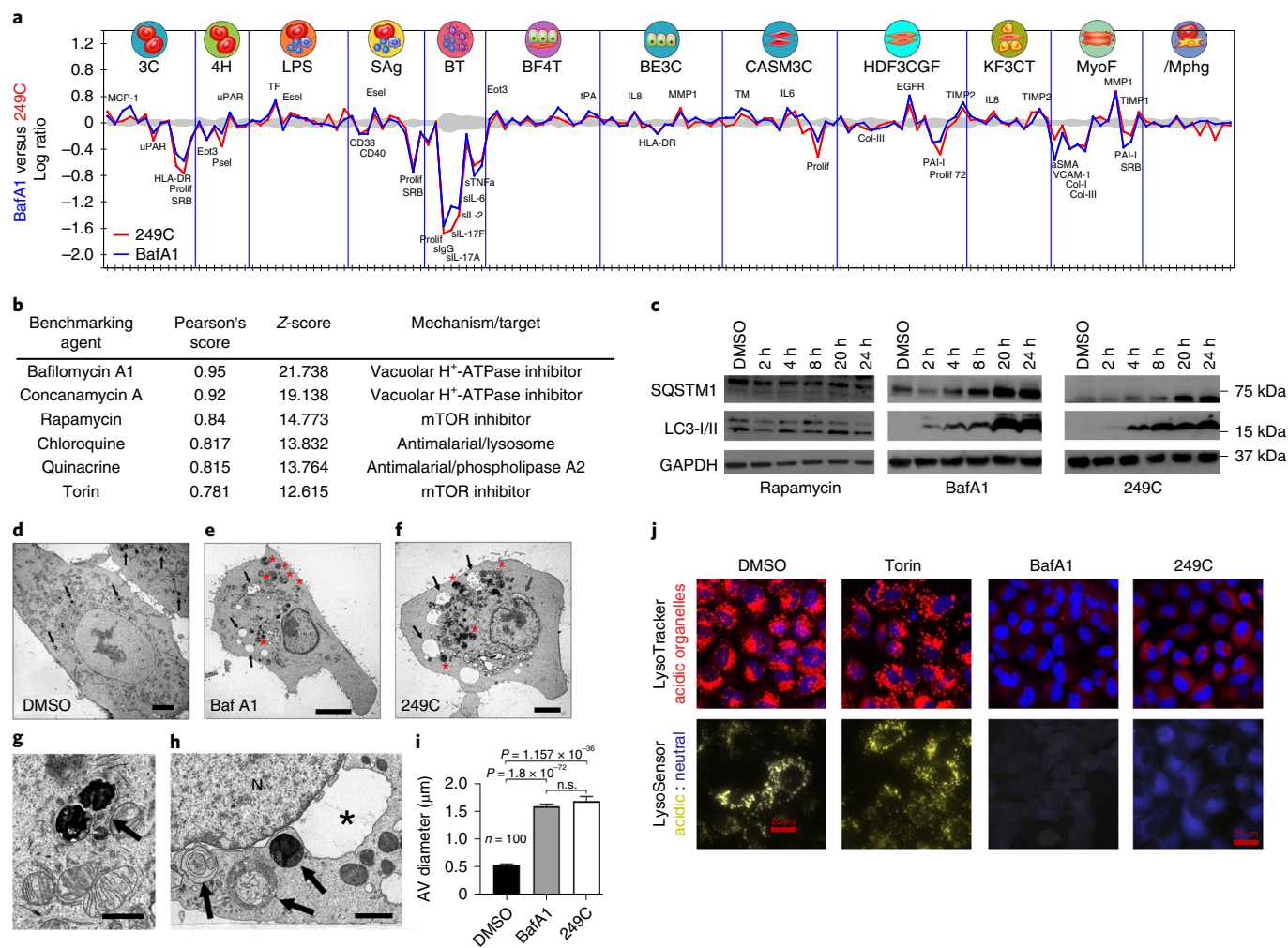


**Fig. 2 | Lead small molecule 249C phenocopies V-ATPase inhibitor BafA1. a**, Overlay of 148 biomarker responses in a panel of 12 primary-cell-based systems for 249C and Bafilomycin A1 (BafA1). BafA1 had the highest similarity out of 4,000 molecules. **b**, Pearson's correlation and Z-scores for observed phenotypes of 249C in comparison to known database drugs (Supplementary Table 4). **c**, Treatment with 249C or the autophagy inhibitor BafA1, but not with the autophagy inducer rapamycin, resulted in upregulation of autophagy markers SQSTM1/p62 and LC3-I/II over time (full-length blot available in Source data Fig. 2). **d-f**, Representative electron micrographs of A549 cells treated with **(d)** the DMSO vehicle, **(e)** BafA1, or **(f)** 249C. Arrows in **d** indicate very densely staining phagosomes/lysosomes; arrows in **e** and **f** indicate large, clear vacuoles within the cells that are absent in **d**; red asterisks in **e** and **f** large multivesicular autophagic vesicles (AVs). **g**, Shows two of these structures at higher magnification from a DMSO-treated cell (arrow). **h**, Multivesicular AVs in a cell treated with 249C (arrows). The nucleus (N) in this cell exhibits a greatly distended portion of the nuclear envelope (asterisk) that resembles the large vacuoles seen in the cytoplasm of BafA1- and 249C-treated cells. **i**, Quantification of mean  $\pm$  s.e.m. of the size of the multivesicular AVs from counts of cell treated with DMSO, BafA1 ( $P = 1.836 \times 10^{-72}$ ) and 249C ( $P = 1.157 \times 10^{-36}$ ). Two-sided *t*-test,  $n = 124$ . n.s., not significant. **j**, Treatment with the autophagy inhibitor BafA1 and 249C decreased staining of acidic organelles (red; LysoTracker) and resulted in an increase in lysosomal pH (yellow, acidic; blue, neutral; LysoSensor) relative to the DMSO control and the autophagy inducer Torin1 in A549 cells (KRASG12S). Representative images from  $n > 3$ . Scale bars: **d-f**, 5  $\mu$ m; **g,h**, 1  $\mu$ m.

$V_1$  region. In addition to blocking acidification, both 249C and BafA1 blocked ATP hydrolysis of intact mammalian V-ATPase purified from pig kidneys (but not yeast; Supplementary Fig. 5) at concentrations as low as 1  $\mu$ M, as measured by a standard biochemical V-ATPase activity assay (Fig. 3d). To directly measure binding of 249C to V-ATPase, we performed bio-layer interferometry (BLI) with both the purified intact mammalian V-ATPase complex and the recombinant ATP6V<sub>H</sub> subunit using biotinylated 249C loaded onto streptavidin sensors (Fig. 5e,f), which revealed binding with nanomolar affinities ( $K_d$ : complex = 23 nM; H sub = 501 nM) (Fig. 3e,f and Supplementary Fig. 6). Altogether, these results establish that 249C directly binds to and inhibits mammalian V-ATPase.

**249C preferentially kills mouse embryonic fibroblasts bearing specific KRAS mutations.** The most frequent KRAS mutations across all human cancers occur at codons 12 or 13 with replacement of glycine to other amino acids: G12D (35%); G12V (24%); and G13D (13%)<sup>29</sup>. To test the impact of 249C on cells carrying individual Ras/Raf mutations, we measured the potency of 249C against immortalized mouse embryonic fibroblasts (MEFs) genetically engineered to be 'Ras-less' with subsequent stable transduction of human wild-type (WT) or mutant KRAS/BRAF isoforms<sup>30</sup> obtained from the National Cancer Institute. The MEF system: (1) permits comparison of individual KRAS mutations in the absence of other oncogenic drivers found in cancer cells; (2) is routinely and widely used to examine the selectivity of KRAS-directed therapies<sup>31-33</sup>; and

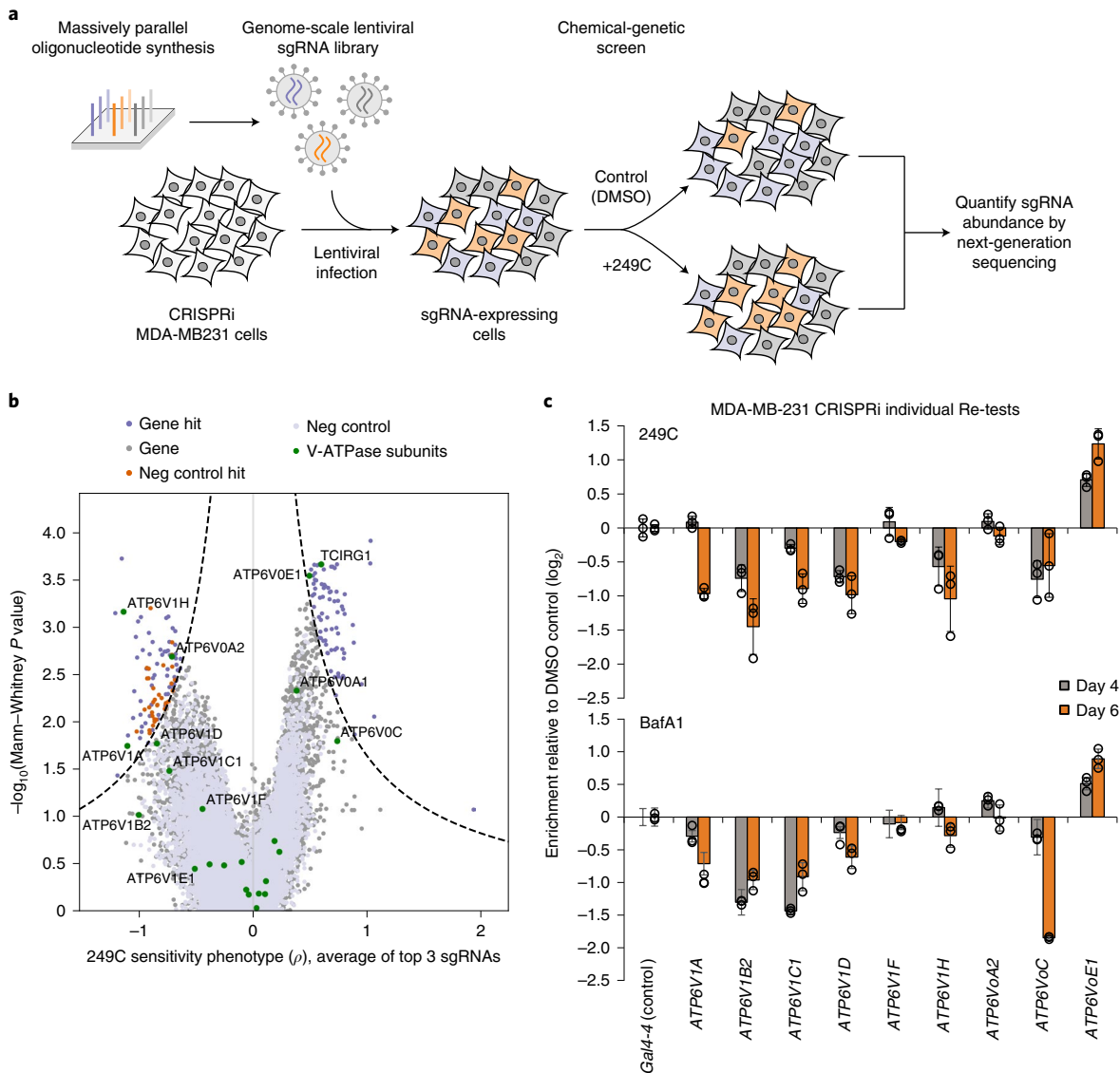


**Fig. 3 | Genome-scale chemical-genetic CRISPRi screen implicates V-ATPase as the molecular target of 249C.** **a**, Schematic illustration of the genome-wide CRISPRi chemical-genetic screen. **b**, Volcano plot of 249C sensitivity phenotype from genome-scale CRISPRi screen in MDA-MB-231 cells. Phenotypes from sgRNAs targeting the same gene were collapsed into a single sensitivity phenotype for each gene using the average of the top three scoring sgRNAs and assigned a  $P$  value using a two-sided Mann-Whitney U test of all sgRNAs targeting the same gene as compared to the non-targeting controls. Negative control genes were randomly generated from the set of non-targeting sgRNAs. Dashed line represents discriminant score  $\geq 7$ , calculated as phenotype Z-score  $\times -\log_{10}(P \text{ value})$ , with the Z-score defined from the standard deviation of the negative control genes. V-ATPase genes are shown in green. **c**, Internally controlled individual re-tests for 249C and BafA1 sensitivity assays performed with sgRNAs targeting (*ATP6V1*-A, B2, C1, D, F, H and *ATP6Vo*-A2, C, E1) or a non-targeting control sgRNA (*Gal4-4*) in MDA-MB-231 CRISPRi cells. Cells transduced with the sgRNA expression constructs (marked with BFP) were left untreated or treated with 249C/BafA1 4 days after transduction. Enrichment of sgRNA-expressing cells was measured after treatment on the days indicated by flow cytometry as the enrichment of BFP ( $n=3$ ). Data presented are mean  $\pm$  s.d. for replicate infections and treatments ( $n=3$ ) (Supplementary Fig. 4 and Supplementary Tables 5 and 6).

(3) is used to study autophagy<sup>34</sup>. Strikingly, 249C exhibited increased potency against cells expressing *KRAS/BRAF* mutants rather than the WT genes (Fig. 5a). Moreover, potency depended on the identity of the mutant ( $IC_{50}$  values: WT (1.25  $\mu$ M); G13D (0.07  $\mu$ M); G12V (0.15  $\mu$ M); G12S (0.23  $\mu$ M); G12D (0.3  $\mu$ M); Q61L (0.31  $\mu$ M); G12C (0.44  $\mu$ M); Q61R (0.55  $\mu$ M); and *BRAF* V600E (0.11  $\mu$ M)), suggesting that susceptibility to V-ATPase inhibition differs across *KRAS/BRAF* mutants (Fig. 5a and Supplementary Fig. 1c; G13D,  $P < 0.05$ ). Treatment with BafA1 showed similar profiles except for G12C, G12D, and Q61L, whereas the HCQ analog (DC661) and the autophagy inducer (CMA) showed substantially different profiles relative to 249C, and the *KRAS*G12C inhibitor (AMG510)

specifically killed cells expressing *KRAS*G12C. Of note, human and mouse *ATP6V<sub>1</sub>H* share 98.55% sequence identity; of the remaining, five amino acids are similar.

**249C inhibits macropinocytosis in a *KRAS*-mutant-dependent manner.** To investigate the mechanism of mutant selectivity of 249C, we explored how 249C impacts four main phenotypes in MEFs expressing *KRAS/BRAF* mutants: (1) lysosomal pH; (2) dependence on V-ATPase activity; (3) apoptosis; and (4) levels of MP.

Cancer cells are reported to have lower lysosomal pHs than untransformed cells, and stably expressing oncogenic *KRAS*G12V in untransformed cells is sufficient to decrease lysosomal pH<sup>35</sup>. To test

this in our system, we stained MEFs bearing *KRAS* WT and *KRAS*/*BRAF* mutants with a pH-sensitive dye and discovered that MEFs bearing *KRASG13D* exhibited the most acidic lysosomes (basal levels) compared with WT or other mutants (Fig. 5b). Thus the mere expression of *KRASG13D* versus WT (or some of the other mutants) renders the lysosomes in these cells more acidic. Since V-ATPases are responsible for acidifying lysosomes, these data indicate that *KRASG13D* cells could bear more biochemically active V-ATPase. As expected, treatment with 249C or BafA1 increased the pH of lysosomes of *KRASG13D* MEFs (Fig. 5b, Supplementary Fig. 7). To next test if these differences in lysosomal pH were caused by differential dependence on V-ATPase activity, we measured lysosome acidification in MEFs bearing WT *KRAS* or *KRAS*/*BRAF* mutants using FITC-Dextran as in Fig. 3f. Untreated *KRASG13D* MEFs accumulated the most FITC in their lysosomes, indicative of more active V-ATPase and thus more acidic lysosomes. As expected, 249C inhibited V-ATPase-dependent proton transport in most MEFs, as measured by ATP-dependent fluorescence quenching of FITC-loaded lysosomes (Fig. 5c and Supplementary Fig. 8). Strikingly, 249C inhibited fluorescence quenching most strongly in *KRASG13D* MEFs. V-ATPase inhibition and increased pH might subsequently halt the degradative process in lysosome-autophagic vesicle (AV) fusion. Indeed, when we analyzed these MEFs by transmission electron microscopy, we found considerably higher AV diameters in MEFs bearing *KRASG13D*, *KRASG12V*, or *BRAFV600E* after 249C treatment compared with *KRAS* WT and other mutants, probably owing to autophagic flux blockade (Fig. 5d,e). Next, as an orthogonal measure of cell death, when we assessed these MEFs by flow cytometry, we found that 249C induced apoptosis in MEFs bearing *KRASG13D* ( $P=0.0009$ ), *KRASG12V* ( $P=0.002$ ), and *BRAFV600E* ( $P=0.001$ ),

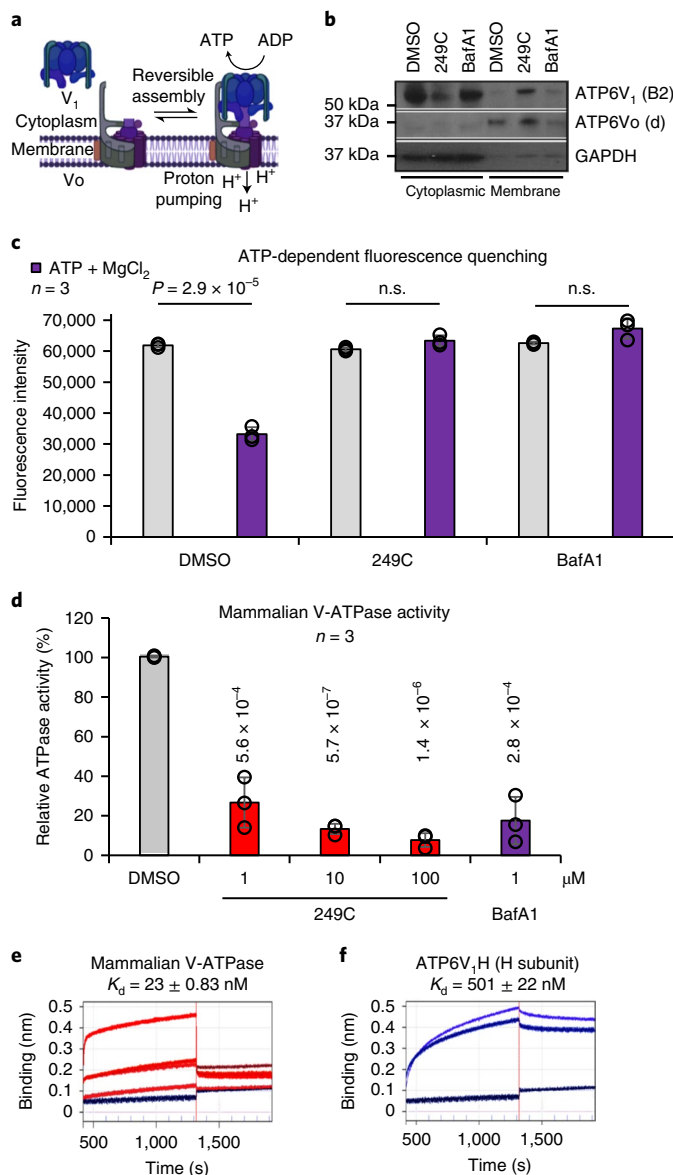
but less so in MEFs expressing *KRAS* WT (Fig. 5f). Similarly, 249C significantly increased apoptosis in *KRAS*-mutant cancer cells as compared to *KRAS* WT cells (Supplementary Fig. 8g).

V-ATPase-dependent lysosome acidification is essential for autophagy and MP. We next tested if MP activity varies across different Ras/Raf-mutant cells and whether such variations correlated with sensitivity to 249C. *KRASG13D* cells (followed by *KRASG12V* cells) cells had the highest levels of basal MP (absolute values) measured by uptake of fluorescently labeled dextran (Supplementary Fig. 8a) suggestive of higher V-ATPase activity attributable to the identity of the *KRAS* mutant in these cells. Reciprocally, treatment with 249C caused the strongest inhibition of MP in MEFs bearing *KRASG13D* (94%) and *BRAFV600E* (90%), in agreement with the low  $IC_{50}$  of cells bearing these mutants (Fig. 5g,h; *KRASG12V* (73%)). Even though *KRASG13D* is not associated with the highest proliferation rate, we speculate that of all available metabolic pathways, *KRASG13D* cells derive a particularly high fraction of their energy from MP/autophagy and thus are particularly reliant on V-ATPase for survival.

**Sensitivity to 249C varies with MAPK, IGF1R, and EGFR signaling.** We next asked whether differential dependence on other signal transduction pathways in different *KRAS*-mutant cells

#### Fig. 4 | Validation of functional biochemical and biophysical effects of 249C on V-ATPase activity.

**a**, Model of the reversible assembly of V-ATPase. Cytosolic  $V_1$  subunits are depicted in blue and membrane  $V_0$  subunits in purple. Upon V-ATPase assembly, ATP is hydrolyzed to ADP accompanied by proton ( $H^+$ ) pumping and luminal acidification (decrease in pH). Created with BioRender (<https://biorender.com>). **b**, HEK293T cells were treated with 249C or BafA1 and cell homogenates were prepared, separated into membrane and cytosolic fractions and analyzed by Western blotting using antibodies against subunit B2 as a measure of the  $V_1$  domain and subunit  $V_{od}$  as a loading control for the membrane fraction, and GAPDH as a loading control for the cytosolic fraction (Methods). The amount of subunit B2 present in the membrane fraction indicates the amount of assembled V-ATPase. A representative Western blot is presented (full-length blot available in Source data Fig. 4). **c**, After 1 h of 249C or BafA1 treatment, HEK293T cells were allowed to take up FITC-Dextran by endocytosis, and the dye was chased to the lysosomal compartment (Methods). Cells were mechanically lysed, and a fraction containing FITC-Dextran-loaded lysosomes was isolated by sedimentation centrifugation. Fluorescence was measured over time to assess pH-dependent quenching following addition of 1 mM magnesium-ATP (predetermined). ATP-dependent fluorescence quenching was not observed for 249C- or BafA1-treated samples. Representative of five individual experiments with  $n=3$  for each is presented (mean  $\pm$  s.d.). **d**, Mammalian V-ATPase activity measured in the absence and presence of 1  $\mu$ M 249C and 1  $\mu$ M BafA1. Data shown are mean  $\pm$  s.d.,  $n=3$ . **e**, f, BLI of the entire mammalian V-ATPase complex (**e**; association protein concentrations: 30, 60, 120, 240 nM) and the individual human H subunit (ATP6V<sub>1</sub>H) (**f**; association protein concentrations, 16,800 and 21,000 nM) against biotinylated 249C loaded onto streptavidin sensor tips. A reference sensor was subtracted from the signal to blank the system. The ForteBio Octet software on the BLI system was used to calculate  $K_d$ . The V-ATPase complex:  $K_d=23 \pm 0.83$  nM; H subunit:  $K_d=501 \pm 22$  nM. Representative raw traces are presented from two independent experiments. See Supplementary Fig. 5f for experimental schematic.



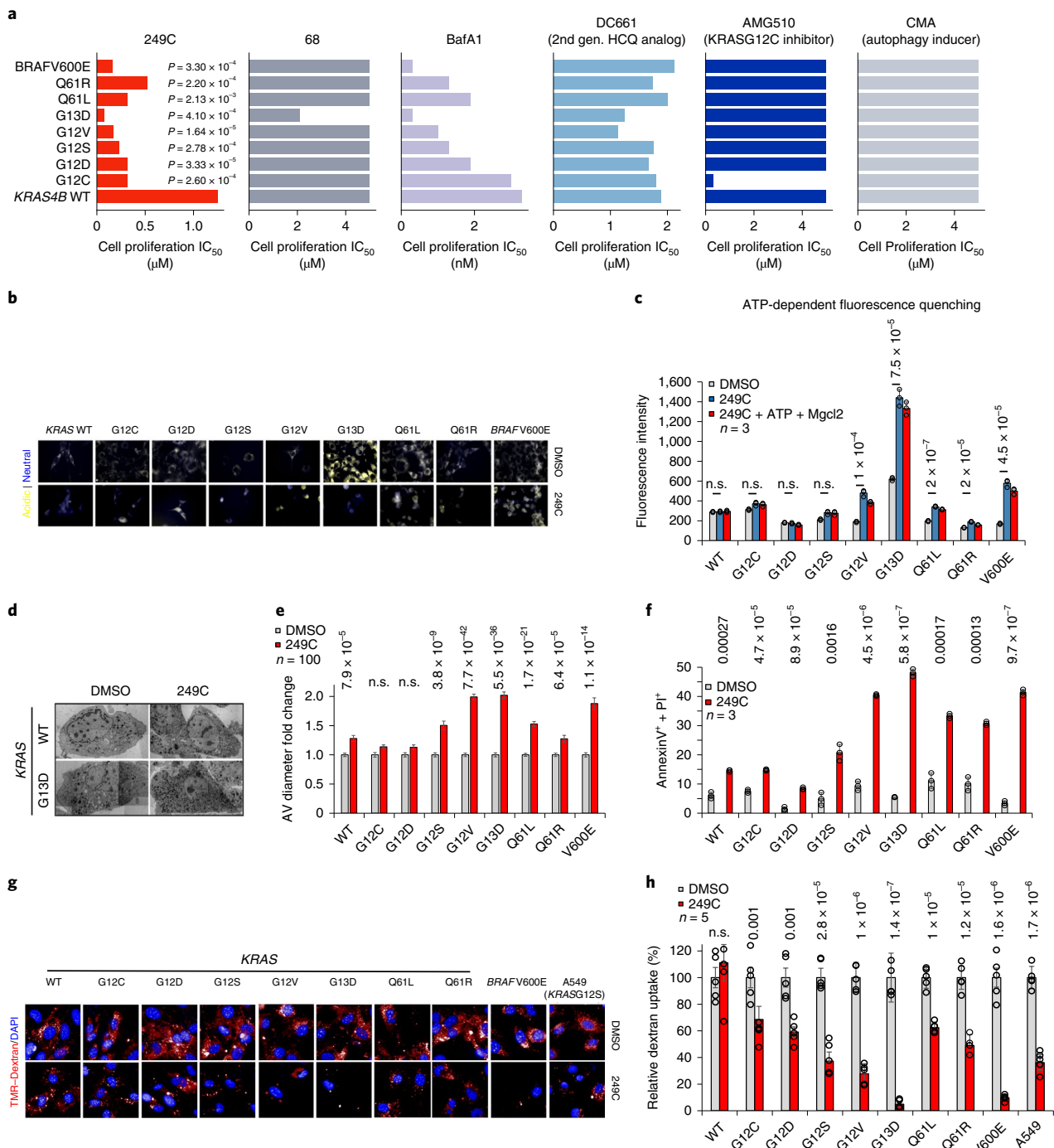


**Fig. 5 | 249C differentially inhibits fibroblasts bearing mutations in *KRAS* and *BRAF* via inhibition of lysosomal pH, V-ATPase activity, and macropinocytosis. **a****, MEFs bearing only single point mutations in human *KRAS*/*BRAF* treated with 249C. IC<sub>50</sub> values: *KRAS* WT (1.25 µM); G13D (0.07 µM); G12V (0.15 µM); G12S (0.23 µM); G12D (0.3 µM); Q61L (0.31 µM); G12C (0.44 µM); Q61R (0.55 µM); and for *BRAF*V600E (0.11 µM). *P* values calculated relative to WT cells treated with 249C. Molecule 68 shown for comparison. Cell proliferation assays of stable cell lines treated with V-ATPase inhibitors 249C and BafA1, HCQ analog (DC661), *KRAS*G12C inhibitor (AMG510) and autophagy inducer (CMA). Each bar represents the mean of *n* = 3 biological replicates; two-sided *t*-test with no adjustments for multiple comparisons. Note, nM used for BafA1. IC<sub>50</sub> > 5 µM were not determined and axes are truncated for clarity. **b**, Basal levels of pH (yellow, acidic; blue, neutral; LysoSensor) in MEFs. Representative images from *n* > 3 (Supplementary Fig. 8). **c**, After 2 h of 249C treatment (or DMSO), FITC-Dextran-loaded lysosomes were isolated from MEFs as in Fig. 3f (see also Supplementary Fig. 8 for DMSO + ATP + MgCl<sub>2</sub> values). Representative of two individual experiments with *n* = 3 (mean ± s.d.); two-sided *t*-test. **d**, Representative electron microscopy images for MEF *KRAS* WT and G13D showing multivesicular AVs after 250 nM 249C treatment for 20 h. Scale bars, 5 µm. Electron microscopy images were stitched together from multiple smaller frames with differences in contrast. **e**, Mean fold change (± s.e.m.) of AV diameter (µm) in MEFs counted on electron microscopy images before and after treatment. *n* = 100 cells per condition; two-sided *t*-test. **f**, Treatment with 100 nM 249C followed by quantification of double-positive Annexin-V<sup>+</sup>/PI<sup>+</sup> cells by flow cytometry at 48 h relative to DMSO controls. Representative of three independent experiments; two-tailed Student's *t*-test. **g**, Fluorescence micrographs showing TMR-dextran uptake after 249C treatment. **h**, Quantification of TMR-dextran uptake. For each cell line, DMSO is set at 100%. The number of objects per nucleus was quantified using high-content imaging software (*n* = 3) data are mean ± s.d.; two-tailed Student's *t*-test.

contributes to the mutant specificity of 249C and whether such dependencies could be exploited for combination therapies. We first evaluated synergy between inhibitors of the MAPK signaling pathway and 249C, since concurrent inhibition of ERK1/2 and autophagy has been reported to synergistically suppress the growth of *KRAS*-mutant cells<sup>36</sup>. Using MEFs and cancer cell lines, we performed co-treatment with 249C and the following MAPK pathway inhibitors: AMG510 (*KRASG12C*); Dabrafenib (*BRAFV600*); Trametinib (MEK1/2); and SCH772984 (ERK1/2) (Supplementary Fig. 9a). As anticipated, *KRASG12C*-mutant lines were sensitive to *KRASG12C*-specific inhibition via AMG510, which was heightened when combined with 249C (Supplementary Fig. 9b). Also, as expected, the *BRAFV600E*-mutant lines were sensitive to *BRAFV600* inhibition via Dabrafenib, which was heightened when combined with 249C (Supplementary Fig. 9c). Finally, Trametinib (MEKi) (Supplementary Fig. 9d) and SCH772984 (ERKi) (Supplementary Fig. 9e) alone modestly decreased proliferation in MEFs expressing *KRAS* mutants and selected cancer cell lines with *KRAS* mutations. Co-treatment with 249C led to further decreased viability, especially at increased concentrations, with effects ranging from additive to mildly synergistic in different cell lines, suggesting that 249C-treated cells may transduce varying levels of signaling via the MAPK pathway. Thus, the addition of 249C could sensitize cells bearing less sensitive *KRAS* mutants to MAPK pathway inhibitors, expanding the potential therapeutic relevance of 249C. For example, Panc1 cells are not particularly sensitive to Trametinib individually, but respond well when combined with 249C (Supplementary Fig. 9d).

We next also evaluated signaling through IGF-1R using an IGF-1R-specific inhibitor, AG-1024. MEFs bearing *KRASG12V* or *KRASG13D* were insensitive to AG-1024, which is likely due to a lack of signaling through this pathway (Supplementary Fig. 10a). By comparison, MEFs expressing WT *KRAS* and other mutants (G12C, G12D, G12S, Q61L, Q61R, and V600E) were sensitive to inhibition, indicating that they can readily signal through the insulin signaling pathway, which can promote cell proliferation (Supplementary Fig. 10b). Thus, we speculate that upon V-ATPase inhibition, cells bearing WT *KRAS* and other mutants could signal through an alternative pathway for survival, but cells bearing *KRASG12V* and *KRASG13D* cannot rely on the insulin pathway.

Finally, we explored the effect of EGFR inhibition using Erlotinib. Consistent with previous reports<sup>37–40</sup>, we found that EGFRi was strongest for cells expressing *KRASG13D* and WT in both MEFs and SW48 cells, indicating their dependence on EGFR signaling, whereas other mutants were not as responsive (Supplementary Fig. 10c,d). Since *KRASG13D* has been suggested to maintain dependence on EGFR signaling when compared with other *KRAS* alleles, we investigated the effects of 249C treatment on EGFR localization via immunofluorescence. We found that in 249C-treated *KRASG13D* cells, EGFR localized predominantly in a punctate manner, likely in vesicles, but in cells expressing WT *KRAS* and other mutants the staining pattern was diffuse (Supplementary Fig. 10).

Cells bearing *KRAS* WT and mutants other than *KRASG12V*, *KRASG13D*, and *BRAFV600E* appear to have alternative signaling capabilities that allow these cells to survive in the presence of 249C. By contrast, for the sensitive mutants, 249C appears to target a composite signaling ‘Achilles’s heel’ for the sensitive mutants.

### 249C inhibits tumor growth in vivo with minimal toxicity.

Finally, to test whether 249C could inhibit autophagy and attenuate the growth of mutant *KRAS*-dependent cancers as a single agent in vivo, we evaluated 249C in a mouse xenograft model of lung cancer (NSCLC, A549). In brief, we injected mutant *KRAS* A549 (G12S) cells into the flanks of athymic mice to establish xenografts, randomly assigned mice to vehicle control ( $n=7$ ) or 249C-recipient groups ( $n=7$ ; 10 mg kg<sup>-1</sup>) with twice daily intraperitoneal (i.p.) injections, and recorded tumor volume and body weight over time.

During the course of the study, all mice survived but tumor volume was significantly lower in 249C-treated mice (Fig. 6a;  $P=2.9 \times 10^{-7}$ ). We subsequently killed all mice and excised their tumors for further investigation. Tumor mass was lower in the 249C-treated group (Fig. 6b;  $P=5.3 \times 10^{-6}$ ), and tumors from mice treated with 249C showed upregulation of LC3-I/II, as assessed by immunoblotting, indicative of inhibition of autophagic flux (Supplementary Fig. 11a). Pharmacokinetic studies revealed that after 4 h, a safe maximum concentration of 20  $\mu$ M of 249C was detected in blood (or plasma) of mice, confirming metabolic stability (Supplementary Fig. 11). Furthermore, 150 mg kg<sup>-1</sup> of 249C was determined to be the maximum tolerated dose in mice and none of the following changed in either group: (1) body weight (Fig. 6c); (2) internal organ tissue weights; and (3) blood cell counts (Supplementary Fig. 11). This suggests a lack of toxicity from treatment; yet even a dose as low as 10 mg kg<sup>-1</sup> is sufficient for antitumor activity.

To explore the relationship between individual *KRAS* mutants and 249C sensitivity in vivo, we used a colon cancer (SW48) xenograft model with a set of colon cancer cell lines that differ in *KRAS* mutation status but are otherwise genetically matched. Stable derivatives of the SW48 cell line were derived by introducing a *KRASG12D*, *KRASG12V*, or *KRASG13D* point mutation via recombinant adeno-associated viral (rAAV) gene-editing technology previously reported<sup>41</sup>. To compare *KRAS* mutants in a cancer relevant system, four cell lines: (SW48, SW48 *KRASG12D*/+, SW48 *KRASG12V*/+, and SW48 *KRASG13D*/+) were injected into athymic mice and 14 days of treatment (10 mg kg<sup>-1</sup> 249C or vehicle control, i.p.;  $n=5$  for all arms) was started when the average tumor volume reached approximately 100–200 mm<sup>3</sup> following random segregation into groups. As before, *KRASG13D* tumors were most sensitive to 249C both in vitro and in vivo (Fig. 6d,e). On day 21, the antitumor activity of 249C, presented as treatment/control, was 18% for SW48 *KRASG13D*/+ ( $P=9.6 \times 10^{-6}$ ), 55% for SW48 *KRASG12V*/+ ( $P=0.005$ ), 75% for SW48 *KRASG12D*/+ ( $P=0.79$ ), and ~100% for parental SW48 ( $P=0.97$ ), and the corresponding tumor growth inhibition was 82%, 45%, 25%, and 0%, respectively (Fig. 6e). Changes in tumor volume are presented for animals bearing isogenic SW48 cells: parental/*KRAS* WT (Fig. 6f), *KRASG12D*/+ (Fig. 6g), *KRASG12V*/+ (Fig. 6h), *KRASG13D*/+ (Fig. 6i). Note that SW48 tumors with different *KRAS* variants show different basal growth rates, as reported previously (<https://tiny.cc/horizondiscovery>). Nonetheless, these data indicate that replacement of a single WT allele with a mono-allelic *KRASG13D*/+ mutation is sufficient to significantly and drastically alter sensitivity to 249C and result in tumor regression in a xenograft model. Further, no significant changes in body weight of the mice were observed during the study (Fig. 6j).

To further evaluate the potential for secondary effects and adverse events in human cells, which is key to preventing phase I failures, we assessed the effect of 249C on hERG. The autophagy inhibitors CQ and HCQ are known to induce a high risk of cardiac electrocardiogram long QT syndrome (LQTS) through inhibition of hERG. In a side-by-side comparison, 249C showed no inhibition of hERG at 30  $\mu$ M (0% inhibition) (Fig. 6k), whereas HCQ (~60% inhibition), BafA1 (35% inhibition), and DC661 (100% inhibition) all showed substantial inhibition (Supplementary Fig. 11), indicating less risk and a sizeable therapeutic window for 249C<sup>18,42</sup>. Finally, we used BioMAP Phenotypic Safety and Toxicology profiling<sup>43</sup> to screen for adverse effects. In human primary cells relevant to physiology, BafA1 showed toxicity in two categories but 249C was determined to have no adverse events across over 100 biomarker readouts, an endorsement of its candidacy to progress into the clinic (Fig. 6l). Collectively, these data indicate that 249C is efficacious in inhibiting tumor growth with minimal side effects (Supplementary Fig. 12) in our investigations thus far, establishing in vivo proof-of-concept for targeting autophagy/MP/lysosomal acidification with 249C in





bridging of rotor ( $V_o$ ) and stator ( $V_i$ ) complexes and physically prevent ATP-driven rotation. 249C may alter  $V_i$ - $V_o$  bridging by binding to ATP6V<sub>1</sub>H. The physical coupling model proposed here is in alignment with previous reports of blocking V-ATPase using BafA1 and/or ConcanamycinA (ConA)<sup>48,49</sup>.

A striking feature of 249C is the selectivity for *KRAS* mutants, which we established using three separate systems: (1) a panel of 53 established cancer cell lines (Fig. 1d,c); (2) MEFs expressing specific *KRAS* alleles (Fig. 5a) and; (3) four SW48 colon cancer cells/xenografts that differ in *KRAS* mutation status but are otherwise genetically matched (isogenic) (in vitro (Fig. 6d,e) and in vivo (Fig. 6f-i)). Together, these three systems provide consistent and complementary evidence for the selectivity of 249C for *KRAS*G13D/G12V and highlight a fundamental vulnerability of *KRAS*G13D/G12V mutant cells that has not been reported in this context before.

This selectivity was not explained by differences in V-ATPase localization with different *KRAS* mutants (Supplementary Fig. 8), as might have been expected from previous reports<sup>10</sup>. Instead, this selectivity appears to arise from multiple converging factors. First, *KRAS*G13D and *KRAS*G12V cells have particularly high basal levels of MP and low lysosomal pH, suggesting that these cells derive a larger fraction of their energy from degradative processes such as autophagy and MP and thus are particularly sensitive to V-ATPase inhibition. Second, cells expressing *KRAS* alleles other than *KRAS*G13D or *KRAS*G12V appear to derive proliferative signaling from additional pathways including the IGF-1R pathway, which may allow these cells to better withstand the presence of 249C. Finally, *KRAS*G13D cells rely more strongly on EGFR signaling for growth, and 249C treatment disrupts EGFR localization, removing this pro-proliferative pathway.

Additional factors may contribute to the selectivity of 249C. For example, V-ATPase interacts with the Ragulator, which regulates mTORC1 activation and autophagy<sup>50</sup>. Thus, in addition to inhibiting autophagy and MP, 249C may also disrupt compensatory mTORC1 signaling that normally occurs in these situations. Cells expressing 249C-insensitive mutants like *KRAS*G12D and *KRAS*G12C may also have alternative metabolic signaling pathways that promote survival, whereas cells expressing *KRAS*G13D, which derive most of their energy from lysosomal degradative processes, do not. In addition, differential changes in cellular pH from 249C across different *KRAS* mutants may affect downstream transcription factors differentially, which may further contribute to the inability of cells expressing *KRAS*G13D or *KRAS*G12V to engage other survival-promoting signal transduction pathways. It may be interesting to deconvolve how cells expressing *KRAS*G12V or *BRAF*V600E, which are sensitive to the changes in pH caused by 249C, differ in their signaling requirements from cells expressing *KRAS*G13D.

249C differs from known V-ATPase/autophagy inhibitors in both mechanism and pharmacology. Antifungal V-ATPase inhibitors, such as BafA1 and ConA, target ATP6VoC, and other autophagy inhibitors, such as the antimalarials HCQ and CQ, act through a different target, PPT1. While both antifungals and antimalarials have potential therapeutic activity, their clinical utility is hampered by toxicity. BafA1 and ConA have been relegated as laboratory compounds, and HCQ and CQ show substantial off-target activity on hERG. By contrast, 249C shows minimal cytotoxicity when compared with BafA1 and minimal inhibition of hERG while maintaining nanomolar potency. Further, BafA1 was first isolated in 1983 and to date no clinical trials have been launched. By contrast, 249C has already entered phase I clinical trials.

Available evidence, such as differences in signaling in cells expressing different Ras mutants<sup>36,51-53</sup>, increasingly suggests that there may not be a single anti-Ras therapeutic approach for all Ras-mutant cancers; instead, mutation-specific therapeutic strategies must be deployed for different Ras mutations. While the emergence of the covalent *KRAS*G12C inhibitor being developed

by Amgen has garnered enthusiasm, there remains a pressing need for therapeutic strategies targeted at cancers driven by other *KRAS* mutations, especially given the dismal outcomes for patients with cancers driven by mutations in *KRAS* codon 13<sup>54,55</sup>. The G13D and G12V mutations account for 13% and 24% of *KRAS* mutations across all human cancers, respectively. Thus, 249C could become a therapeutic for ~37% of all *KRAS* malignancies. Beyond *KRAS*-driven cancers, autophagy dysregulation has been linked to a wide range of diseases including metabolic disorders, aging, and neurodegenerative diseases<sup>56</sup>, motivating investigation of 249C as a drug candidate for other treatment applications.

## Online content

Any methods, additional references, Nature Research reporting summaries, source data, extended data, supplementary information, acknowledgements, peer review information; details of author contributions and competing interests; and statements of data and code availability are available at <https://doi.org/10.1038/s41587-022-01386-z>.

Received: 2 November 2021; Accepted: 3 June 2022;

Published online: 25 July 2022

## References

- Simanshu, D. K., Nissley, D. V. & McCormick, F. RAS proteins and their regulators in human disease. *Cell* **170**, 17–33 (2017).
- Cox, A. D., Fesik, S. W., Kimmelman, A. C., Luo, J. & Der, C. J. Drugging the undruggable Ras: mission possible? *Nat. Rev. Drug Discov.* **11**, 828–851 (2014).
- Waters, A. M. & Der, C. J. KRAS: the critical driver and therapeutic target for pancreatic cancer. *Cold Spring Harb. Perspect. Med.* **8**, a031435 (2018).
- Hobbs, A. G., Der, C. J. & Rossman, K. L. RAS isoforms and mutations in cancer at a glance. *J. Cell Sci.* **129**, 1287–1292 (2016).
- Choi, A. M., Ryter, S. W. & Levine, B. Autophagy in human health and disease. *N. Engl. J. Med.* **368**, 651–662 (2013).
- Guo, J. Y. et al. Autophagy provides metabolic substrates to maintain energy charge and nucleotide pools in Ras-driven lung cancer cells. *Genes Dev.* **30**, 1704–1717 (2016).
- Efeyan, A., Comb, W. C. & Sabatini, D. M. Nutrient-sensing mechanisms and pathways. *Nature* **517**, 302–310 (2015).
- Mizushima, N., Levine, B., Cuervo, A. M. & Klionsky, D. J. Autophagy fights disease through cellular self-digestion. *Nature* **451**, 1069–1075 (2008).
- Guo, J. Y. & White, E. Autophagy is required for mitochondrial function, lipid metabolism, growth, and fate of KRAS(G12D)-driven lung tumors. *Autophagy* **9**, 1636–1638 (2013).
- Ramirez, C., Hauser, A. D., Vucic, E. A. & Bar-Sagi, D. Plasma membrane V-ATPase controls oncogenic RAS-induced macropinocytosis. *Nature* **576**, 477–481 (2019).
- Rabinowitz, J. D. & White, E. Autophagy and metabolism. *Science* **330**, 1344–1348 (2010).
- Commissio, C. et al. Macropinocytosis of protein is an amino acid supply route in Ras-transformed cells. *Nature* **497**, 633–637 (2013).
- Forgac, M. Vacuolar ATPases: rotary proton pumps in physiology and pathophysiology. *Nat. Rev. Mol. Cell Biol.* **8**, 917–929 (2007).
- Zhao, J., Benlekber, S. & Rubinstein, J. L. Electron cryomicroscopy observation of rotational states in a eukaryotic V-ATPase. *Nature* **521**, 241–245 (2015). May 14.
- Stransky, L., Cotter, K. & Forgac, M. The function of v-ATPases in cancer. *Physiol. Rev.* **96**, 1071–1091 (2016).
- Li, Z. et al. Complete elucidation of the late steps of bafilomycin biosynthesis in *Streptomyces lohii*. *J. Biol. Chem.* **292**, 7095–7104 (2017).
- Rebecca, V. W. et al. PPT1 promotes tumor growth and is the molecular target of chloroquine derivatives in cancer. *Cancer Discov.* **9**, 220–229 (2019).
- Michaud, V. et al. Risk assessment of drug-induced long QT syndrome for some COVID-19 repurposed drugs. *Clin. Transl. Sci.* **14**, 20–28 (2021).
- Rebecca, V. & Amaravadi, R. Emerging strategies to effectively target autophagy in cancer. *Oncogene* **35**, 1–11 (2016).
- Carew, J. S. & Nawrocki, S. T. Drain the lysosome: development of the novel orally available autophagy inhibitor ROC-325. *Autophagy* **13**, 765–766 (2017).
- McAlister, G. C. et al. MultiNotch MS3 enables accurate, sensitive, and multiplexed detection of differential expression across cancer cell line proteomes. *Anal. Chem.* **86**, 7150–7158 (2014).
- Berg, E. L., Kunkel, E. J., Hytopoulos, E. & Plavec, I. Characterization of compound mechanisms and secondary activities by BioMAP analysis. *J. Pharmacol. Toxicol. Methods* **53**, 67–74 (2006).

23. Jost, M. & Weissman, J. S. CRISPR approaches to small molecule target identification. *ACS Chem. Biol.* **13**, 366–375 (2018).
24. Gilbert, L. A. et al. CRISPR-mediated modular RNA-guided regulation of transcription in eukaryotes. *Cell*. **154**, 442–451 (2013).
25. Horlbeck, M. A. et al. Compact and highly active next-generation libraries for CRISPR-mediated gene repression and activation. *eLife* **5**, e19760 (2016).
26. Gilbert, L. A. et al. Genome-scale CRISPR-mediated control of gene repression and activation. *Cell* **159**, 647–661 (2014).
27. Bowman, B. J. & Bowman, E. J. Mutations in subunit C of the vacuolar ATPase confer resistance to bafilomycin and identify a conserved antibiotic binding site. *J. Biol. Chem.* **277**, 3965–3972 (2002).
28. Liberman, R., Bond, S., Shainheit, M. G., Stadecker, M. J. & Forgac, M. Regulated assembly of the V-ATPase is increased during cluster disruption-induced maturation of dendritic cells through a PI-3 kinase/mTOR-dependent pathway. *J. Biol. Chem.* **289**, 1355–1363 (2014).
29. Stolze, B., Reinhart, S., Bullinger, L., Fröhling, S. & Scholl, C. Comparative analysis of KRAS codon 12, 13, 18, 61, and 117 mutations using human MCF10A isogenic cell lines. *Sci. Rep.* **5**, 8535 (2015).
30. Drosten, M. et al. Genetic analysis of Ras signaling pathways in cell proliferation, migration and survival. *EMBO J.* **29**, 1091–1104 (2010).
31. Teng, K. W. et al. Selective and noncovalent targeting of RAS mutants for inhibition and degradation. *Nat. Commun.* **12**, 2656 (2021).
32. Janes, M. R. et al. Targeting KRAS mutant cancers with a covalent G12C-specific inhibitor. *Cell*. **172**, 578–589 (2018).
33. Haza, K. Z. et al. RAS-inhibiting biologics identify and probe druggable pockets including an SII- $\alpha$ 3 allosteric site. *Nat. Commun.* **12**, 4045 (2021).
34. Lock, R. et al. Autophagy facilitates glycolysis during Ras-mediated oncogenic transformation. *Mol. Biol. Cell.* **22**, 165–178 (2010).
35. Webb, B. A. et al. pHLARE: a new biosensor reveals decreased lysosome pH in cancer cells. *Mol. Biol. Cell.* **32**, 131–142 (2021).
36. Hobbs, G. A. et al. Atypical KRAS<sup>G12R</sup> mutant is impaired in PI3K signaling and macropinocytosis in pancreatic cancer. *Cancer Discov.* **10**, 104–123 (2020).
37. McFall, T. & Stites, E. C. A mechanism for the response of KRAS<sup>G13D</sup> expressing colorectal cancers to EGFR inhibitors. *Mol. Cell Oncol.* **7**, 1701914 (2020).
38. McFall, T., Schomburg, N. K., Rossman, K. L. & Stites, E. C. Discernment between candidate mechanisms for KRAS G13D colorectal cancer sensitivity to EGFR inhibitors. *Cell Commun. Signal.* **18**, 179 (2020). Nov 5.
39. McFall, T. et al. A systems mechanism for KRAS mutant allele-specific responses to targeted therapy. *Sci. Signal.* **12**, eaaw8288 (2019).
40. McFall, T. & Stites, E. C. Identification of RAS mutant biomarkers for EGFR inhibitor sensitivity using a systems biochemical approach. *Cell Rep.* **37**, 110096 (2021).
41. Hammond, D. E. et al. Differential reprogramming of isogenic colorectal cancer cells by distinct activating KRAS mutations. *J. Proteome Res.* **14**, 1535–1546 (2015).
42. Trudeau, M. C., Warmke, J. W., Ganetzky, B. & Robertson, G. A. H. E. R. G. A human inward rectifier in the voltage-gated potassium channel family. *Science* **269**, 92–95 (1995).
43. Kleinstreuer, N. C. et al. Phenotypic screening of the ToxCast chemical library to classify toxic and therapeutic mechanisms. *Nat. Biotechnol.* **32**, 583–591 (2014).
44. Aguilera, K. Y. et al. Inhibition of discoidin domain receptor 1 reduces collagen-mediated tumorigenicity in pancreatic ductal adenocarcinoma. *Mol. Cancer Ther.* **16**, 2473–2485 (2017).
45. Ruggeri, J. M. et al. Discoidin domain receptor 1 (DDR1) is necessary for tissue homeostasis in pancreatic injury and pathogenesis of pancreatic ductal adenocarcinoma. *Am. J. Pathol.* **190**, 1735–1751 (2020).
46. Diehl, J. N. et al. The KRAS-regulated kinome identifies WEE1 and ERK coinhibition as a potential therapeutic strategy in KRAS-mutant pancreatic cancer. *J. Biol. Chem.* **297**, 101335 (2021).
47. Wilkens, S., Inoue, T. & Forgac, M. Three-dimensional structure of the vacuolar ATPase. Localization of subunit H by difference imaging and chemical cross-linking. *J. Biol. Chem.* **279**, 41942–41949 (2004).
48. Zoncu, R. et al. mTORC1 senses lysosomal amino acids through an inside-out mechanism that requires the vacuolar H<sup>+</sup>-ATPase. *Science* **334**, 678–683 (2011).
49. Bar-Peled, L., Schweitzer, L. D., Zoncu, R. & Sabatini, D. M. Ragulator is a GEF for the rag GTPases that signal amino acid levels to mTORC1. *Cell* **150**, 1196–1208 (2012).
50. Chung, C. Y. et al. Covalent targeting of the vacuolar H<sup>+</sup>-ATPase activates autophagy via mTORC1 inhibition. *Nat. Chem. Biol.* **15**, 776–785 (2019).
51. Rabara, D. et al. KRAS G13D sensitivity to neurofibromin-mediated GTP hydrolysis. *Proc. Natl Acad. Sci. USA* **116**, 22122–22131 (2019).
52. Yang, J. et al. Elevated expression of the V-ATPase D2 subunit triggers increased energy metabolite levels in Kras<sup>G12D</sup>-driven cancer cells. *J. Cell Biochem.* **120**, 11690–11701 (2019).
53. Zhang, X., Cao, J., Miller, S. P., Jing, H. & Lin, H. Comparative nucleotide-dependent interactome analysis reveals shared and differential properties of KRas4a and KRas4b. *ACS Cent. Sci.* **4**, 71–80 (2018).
54. Er, Tze-Kiong, Chen, Chih-Chieh, Bujanda, Luis & Herreros-Villanueva, Marta Clinical relevance of KRAS mutations in codon 13: where are we? *Cancer Letters* **343**, 1–5 (2014).
55. Hobbs, G. A. & Der, C. J. Binge drinking: macropinocytosis promotes tumorigenic growth of RAS-mutant cancers. *Trends Biochem. Sci.* **45**, 459–461 (2020).
56. Rubinsztein, D. C., Codogno, P. & Levine, B. Autophagy modulation as a potential therapeutic target for diverse diseases. *Nat. Rev. Drug Discov.* **11**, 709–730 (2012).

**Publisher's note** Springer Nature remains neutral with regard to jurisdictional claims in published maps and institutional affiliations.



**Open Access** This article is licensed under a Creative Commons Attribution 4.0 International License, which permits use, sharing, adaptation, distribution and reproduction in any medium or format, as long as you give appropriate credit to the original author(s) and the source, provide a link to the Creative Commons license, and indicate if changes were made. The images or other third party material in this article are included in the article's Creative Commons license, unless indicated otherwise in a credit line to the material. If material is not included in the article's Creative Commons license and your intended use is not permitted by statutory regulation or exceeds the permitted use, you will need to obtain permission directly from the copyright holder. To view a copy of this license, visit <http://creativecommons.org/licenses/by/4.0/>.

© The Author(s) 2022

## Methods

**Cell lines, reagents and proliferation assays.** Most cells were obtained from the American Type Culture Collection (ATCC) and were cultured in ATCC-recommended medium supplemented with 10% fetal bovine serum and 2% antibiotics (penicillin–streptomycin). MDA-MB-231 CRISPRi cells were a gift from H. Goodarzi at UCSF (parent cells from ATCC). MEFs expressing human *KRAS/BRAF* were from the Frederick National Laboratory for Cancer Research, the National Cancer Institute. SW48 cells were obtained from Horizon Disc.

ATCC cell lines: H1944 (CRL-5907), A427 (HTB-53), A549 (CRM-CCL-185), SW1271 (CRL-2177), H292 (CRL-1848), H358 (CRL-5807), H1299 (CRL-5803), H460 (HTB-177), H1703 (CRL-5889), H2170 (CRL-5928), H2452 (CRL-5946), NCI H82 (HTB-175), Calu-3 (HTB-55), H838 (CRL-5844), H1975 (CRL-5908), H1650 (CRL-5883), H28 (CRL-5820), CFPAC-1 (CRL-1918), Capan-1 (HTB-79), Panc 02-13 (CRL-2554), ASPC1 (CRL-1682), Panc1 (CRL-1469), BxPC3 (CRL-1687), MDA-MB-231 (HTB-26), Sk-Br-3 (HTB-30), MCF7 (HTB-22), MDA-MB-436 (HTB-130), HCT116 (CRL-247EMT), Colo201 (CCL-224), N87 (CRL-5822), RKO (CRL-2577), SW48 (CCL-231), CaCO2 (HTB-37), SkMel5 (HTB-70), SKMEL30 (HTB-73), A375 (CRL-1619), A2058 (CRL-11147), DUI145 (HTB-81), PC3 (CRL-3471), U251 (HTB-17), U87 (HTB-14), HL-60 (CCL-240), and HepG2 (HB-8065). LOX IMVI, MeJuso, BT474 and HCC1937 cells were a gift from the Ortiz–Urda lab at UCSF originally sourced from ATCC or as gifts. ES2, OVCAR8, HEYA8, and HEY cells were a gift from the Smith–McCune lab at UCSF originally sourced from ATCC.

BafA1, chloroquine, hydroxychloroquine, and DC661 were from Medchemexpress. Rapamycin was from Selleckchem and Torin was from Fisher. Erlotinib, AG-1024, and MAPK inhibitors were from Selleckchem. DNA transfection into cells was performed with TransIT-LT1 Transfection Reagent (Mirus Bio) by following the manufacturer's recommendations.

Logarithmically growing cells were plated in antibiotic-free medium supplemented with 2% fetal bovine serum at a density of 5,000 cells per well. The next day, cells were treated in triplicates with increasing doses of in-house small molecule inhibitor drugs and a DMSO vehicle control for 3 days and subsequently assessed for cell viability by measurement of ATP with CellTiter-Glo Luminescent Cell Viability Assay (Promega). Signal intensity was read on a Glomax 96 Microplate Luminometer (Promega) with GLOMAX software (v.1.9.3) and percent cell survival was calculated on the basis of the reading of vehicle control cells set as 100% using Excel (2012) and GraphPad Prism (v.6). Each compound was tested a minimum of 2 times with  $n=3$ . All cell proliferation assays (cancer cell lines or MEFs) were done in a similar way.

**Chemical synthesis of 249C.** 249C and other small molecules (~300) were synthesized at UCSF and are covered by patent number PCT/US2017/039806 filed with the United States Patent and Trademark Office. In brief, small molecules to represent diversity in the compound library were synthesized by the synthesis method described in Supplementary Fig. 1. The synthetic route is designed to investigate functional group tolerability around the dihydro-pyrazole pharmacophore; simultaneous optimization was carried out for potency and physico-chemical properties. Analytical evaluation of compounds synthesized is presented in Supplementary Table 3.

**Structure–activity relationship investigation.** Compounds synthesized in this series are potent in multiple cancer cell lines. Most calculated properties meet drug-likeness criteria. Initial compounds are hydrophobic in nature, with relatively high logP and have low polar surface area. The lipophilicity of the compounds can be reduced via the introduction of polar side chains resulting in analogs with more favorable physico-chemical properties, that is drug likeness.

**Mutation analysis in CCLE cell lines.** The CCLE (<https://sites.broadinstitute.org/ccle>) was used to download somatic mutation data for over 1,000 cancer cell lines ((CCLE\_DepMap\_18q3\_maf\_20180718.txt) from CCLE at <https://depmap.org/portal/download/> (2018))<sup>57</sup>. We filtered the data to retain only mutations (single nucleotide variants (SNVs) and indels) detected in 53 cell lines that were included in our viability assays (Fig. 1). Non-coding variants, silent mutations and in-frame insertions were removed, as these were not considered functional. We retained in-frame deletions as these may remove essential binding sites. The Combined Annotation Dependent Database (<https://cadd.gs.washington.edu/>) (v.1.6) was used to assess the predicted functional importance of SNVs, and we retained only variants with CADD Phred scores  $\geq 15$  (ref.<sup>58</sup>). Including these predicted damaging SNVs as well as indels (minus in-frame insertions), we determined the number of times each gene was mutated across the 53 cell lines. Genes with multiple mutations in the same cell line were only counted once. Multiple Wilcoxon rank sum tests were carried out, using the 'lapply' looping function in the R statistical environment, to test for association between presence/absence of mutations in each gene and IC<sub>50</sub> values in each cell line. A Wilcoxon rank sum test was also carried out for Ras/Raf mutations, which included combined mutation data for genes *KRAS*, *NRAS*, *HRAS*, *NFI*, and *BRAF*.

**Mass spectrometric whole proteome analysis.** After treatment with small molecules, A549 cells were trypsinized, lysed in 8 M Urea, 1% SDS, 50 mM Tris

pH 8.5, protease (Complete) and phosphatase (PhosStop) inhibitors, and samples were sent to the Thermo Fisher Center for Multiplexed Proteomics at Harvard to be processed as described<sup>5</sup>. In brief, extracts were purified by trichloroacetic acid precipitation, followed by labeling with tandem mass tags (TMT) reagents (Thermo Fisher), and subsequently desalted by StageTips before LC–MS/MS analysis. Data were collected using an Orbitrap Fusion Lumos mass spectrometer (Thermo Fisher Scientific) coupled with a Proxeon EASY-nLC 1200 LC pump (Thermo Fisher Scientific). For LC–MS/MS analysis, an MS<sup>3</sup>-based TMT method was used as previously described<sup>5</sup>. For mass spectrometry data processing and spectra assignment, an MS2 spectra assignment false discovery rate of less than 1% was implemented by applying the target–decoy database search strategy. To quantify TMT reporter ion intensity, a 0.003  $m/z$  window centered on the theoretical  $m/z$  value of each reporter ion was monitored for ions, and the maximum intensity of the signal to the theoretical  $m/z$  value was recorded. Reporter ion intensities were normalized by multiplication with the ion accumulation time for each MS2 or MS3 spectrum and adjusted on the basis of the overlap of isotopic envelopes of all reporter ions. After the reporter ion signal was extracted, the isotopic impurities of the TMT reagent were corrected using the values specified by the manufacturer. Total signal-to-noise values for all peptides were summed for each TMT channel and all values were adjusted to account for variance and a total minimum signal-to-noise value of 200 was implemented<sup>59,60</sup>.

**MSigDB.** GSEA software (version 4.2.3) and Molecular Signature Database (MSigDB, v.7.4) from <https://www.gsea-msigdb.org/gsea/index.jsp> was used to query the top eight proteins from the Whole Proteome Analysis for Gene Ontology gene sets in NCI-60 cell lines<sup>61,62</sup>.

**BioMAP and benchmarking.** BioMAP assays comprising 12 human primary-cell-based systems (co-cultured cells simulating 12 different disease contexts) were treated in the presence or absence of test agents (known drugs and our 249C compound) as described<sup>63</sup>. All cells were from a pool of multiple donors ( $n=2-6$ ) and collected in accordance with appropriate regulatory protocols. Direct enzyme-linked immunosorbent assay was used to measure selected biomarker level readouts (adhesion receptors, cytokines, enzymes etc.) and activity profiles (normalized datasets) were generated for each test agent. The resulting profiles from biomarker readouts were compared or 'benchmarked' to a known 4,000-molecule database by statistical methods to identify similarities and mechanistic insights described previously<sup>64</sup> to provide Pearson's and Z-scores.

**Immunoblotting.** Protein extracts were prepared from drug-treated cells by lysis on ice for 20 min in M-PER Mammalian Protein Extraction Reagent (ThermoScientific) supplemented with protease and phosphatase inhibitors (Roche). Lysates were centrifuged at 16,000 r.p.m. for 20 min at 4 °C and the supernatants were assessed for concentration via a Bradford assay. Protein extracts (25–50  $\mu$ g) were used for gel electrophoresis followed by immunoblotting onto PVDF membranes. Blots were probed with the following primary antibodies: GAPDH (Thermo Fisher, 1:20,000), Ras (1:1000), SQSTM1 (1:1000) and LC3 (1:1000) (Cell Signaling).

**Electron microscopy.** A549 cells attached to ACLAR film<sup>65</sup> were treated for 24 h with 249C (250 nM) or BafA1 (10 nM) or DMSO as a control. The cells on film were then fixed by immersion in 2% glutaraldehyde in 0.08 M Na-cacodylate buffer, pH 7.3 containing 2 mM CaCl<sub>2</sub> that had been pre-warmed to 37 °C for 1 h with gentle agitation during which the fixative cooled to room temperature. The samples were then rinsed with 0.1 M Na-cacodylate buffer at room temperature, post-fixed with 1% OsO<sub>4</sub> containing 1.5% potassium ferrocyanide in 0.1 M Na-cacodylate buffer for 45 min on ice, rinsed with water, en bloc stained with 3.5% uranyl acetate in water for 1 h at room temperature, dehydrated in ethanol followed by propylene oxide, and embedded in Eponate 12 resin (Ted Pell). Thin sections were cut with a Leica UCT ultramicrotome using a Diatome diamond knife and picked up on Pioloform films on slot grids. The grids were then post-stained with 1% uranyl acetate followed by Sato's lead<sup>66</sup>. Sections were imaged with an FEI T12 TEM equipped with a Gatan U895 4k  $\times$  4k camera at 120 kV (software: DigitalMicrograph (v.3.4.3) and SerialEM (v.3.8.6)). Quantification was performed with custom Python image analysis software. MEFs were processed in a similar way.

**Lysosome staining.** Cells were treated with the respective molecules in two-well chambered coverglass slides at a final concentration of 1  $\mu$ M for 18 h followed by addition of lysosome-specific dyes. LysoTracker Red DND-99 and pH-sensitive LysoSensor Yellow/Blue DND-160 purchased from Thermo Fisher were added to the cells for 1 h at 37 °C along with Hoechst to stain DNA according to the manufacturer's recommendations. Live cell images were captured at 20 $\times$  with a Zeiss spinning disc confocal and TIRF Fura microscope at UCSF's Laboratory for Cell Analysis.

**CRISPR screen.** Genome-scale screens using MDA-MB-231 CRISPRi cells (a gift from H. Goodarzi at UCSF) were performed in a similar manner as previously described<sup>25,67</sup>. For genome-wide knockdown, CRISPRi-v2 sgRNA libraries<sup>25</sup> (targeting 18,905 genes and marked with blue fluorescent protein (BFP)) were transduced into MDA-MB-231 CRISPRi cells at a multiplicity of infection <1 (percentage of

transduced cells 2 days after transduction: ~30%). Cells were maintained in DMEM in 20× T-182.5 flasks for the course of the screen. After transduction, the cells were selected with puromycin for 2 days, at which point transduced cells accounted for 90% of the population assessed as the fraction of BFP-positive cells by flow cytometry. After 1 day of recovery without puromycin, samples at time-point  $t_0$  with a minimum established coverage of >1,000 cells per sgRNA were harvested and the remaining cells were split into two populations for untreated growth (DMSO control) and 249C-treated growth. The cells were maintained in T-182.5 flasks at an average coverage of greater than 1,000 cells per sgRNA for the duration of the screen. For 249C treatment, 525 nM 249C was added to the cells at day 0 and day 5 and removed the following day. Cells were harvested on days 19 (DMSO) and 21 (249C) (6.1 doubling differences between treated and untreated populations). Genomic DNA was isolated and the sgRNA-encoding region was amplified and processed for next-generation sequencing on an Illumina HiSeq 4000 (HiSeq Software Suite v.3.4.0) as described previously<sup>68</sup>. Sequencing reads were aligned to the CRISPRi library sequences, counted, and quantified using the Python-based ScreenProcessing pipeline available at <https://github.com/mhorlbeck/ScreenProcessing><sup>25</sup>. Generation of negative control genes and calculation of phenotypes and Mann–Whitney  $P$  values was performed as described previously<sup>67</sup>. Sensitivity phenotypes ( $\rho$ ) were calculated by calculating the  $\log_2$  change in enrichment of an sgRNA in the treated and untreated samples, subtracting the equivalent median value for all non-targeting sgRNAs, and dividing by the number of population doubling differences between the treated and untreated populations<sup>67–69</sup>. Similarly, untreated growth phenotypes ( $\gamma$ ) were calculated from the untreated and  $t_0$  samples, dividing by the total number of doublings of the untreated population. Phenotypes from sgRNAs targeting the same gene were collapsed into a single sensitivity phenotype for each gene using the average of the top three scoring sgRNAs (by absolute value) and assigned a  $P$  value using the Mann–Whitney test of all sgRNAs targeting the same gene in comparison to the non-targeting controls. For genes with multiple independent transcription start sites (TSSs) targeted by the sgRNA libraries, phenotypes and  $P$  values were calculated independently for each TSS and then collapsed to a single score by selecting the TSS with the lowest Mann–Whitney  $P$  value. Read counts and phenotypes for individual sgRNAs are available in Supplementary Table 3. Gene-level phenotypes are available in Supplementary Table 4. All additional analyses were performed using Python 3.7 using a combination of Numpy (v.1.15.4), Pandas (v.0.25.3), and Scipy (v.1.4.1).

**Individual CRISPR re-tests.** Oligonucleotides encoding sgRNAs targeting the selected genes for individual re-tests were acquired from IDT and cloned into the pCRISPRi-v2 vector (Addgene #84832) backbone followed by DNA transformation, extraction, and sequencing to verify accuracy. The sgRNA expression plasmids were packaged into lentivirus and transduced into MDA-MB231 CRISPRi cells. 5 days after transduction, cells were left untreated (DMSO) or treated with 525 nM of 249C or 30 nM BafA1 for 24 h and assessed for BFP using an LSR II flow cytometer at UCSF's Flow Cytometry Core facility. Enrichment of sgRNA-expressing cells was measured as the enrichment of BFP-positive cells [ $e = \text{fraction(BFP+)} / (1 - \text{fraction(BFP+)})$ ], calculated relative to the DMSO-treated control cells. Experiments were performed in triplicates.

**Subcellular fractionation.** Cytoplasmic and membrane extracts from A549 cells left untreated (DMSO) or treated with 249C (20  $\mu\text{M}$ ) or BafA1 (1.5  $\mu\text{M}$ ) for 2 h were prepared using a Subcellular Protein Fractionation Kit by following the manufacturer's recommendations (Fisher). Fractions were subjected to Western blotting as described above and blotted for ATP6V<sub>1</sub>B2 (a gift from D. Brown at Harvard University, 1:1,000) and ATP6VoD (Abcam, 1:1,000) antibodies.

**Protein purification.** Mammalian V-ATPase complex: the entire V-ATPase complex (800 kDa) was purified as described previously from porcine kidneys<sup>23</sup> using the detergent glycol-diosgenin.

ATP6V<sub>1</sub>H (H subunit): Addgene plasmid #14658 was expressed in Rosetta2(DE3)pLysS cells and induced with isopropyl  $\beta$ -D-1-thiogalactopyranoside. Harvested lysates were loaded onto a GSTrap column and bound protein eluted with reduced glutathione. Thrombin was added to cleave the GST tag followed by loading onto a BioRad SEC650 size-exclusion column (Supplementary Fig. 5).

**Bio-layer interferometry studies for binding affinity determination.** Biotinylated 249C was diluted in phosphate-buffered saline (PBS) + 0.05% Tween + 0.2% bovine serum albumin (BSA), pH 7.4 and loaded onto Octet Streptavidin (SA) Biosensors (ForteBio) by following the manufacturer's recommendations on an Octet RED384 machine (ForteBio, PALL Octet System). Biotin–249C immobilization was checked via Octet Software before introduction of the entire V-ATPase complex and the individual H subunit protein diluted in blocking buffer (1× PBS + 0.05% Tween 20 + 0.2% BSA + 10  $\mu\text{M}$  Biotin) to eliminate non-specific binding. A reference sensor was subtracted from the signal to blank the system. The ForteBio Octet Software (v.12) on the BLI system was used to calculate the  $K_d$  values. Graphical output from the Octet Software of representative data from two independent experiments is presented.

**Proton pumping assay in mammalian cells.** HEK293T cells were either left untreated (DMSO control) or treated with 10.5  $\mu\text{M}$  249C or 0.5  $\mu\text{M}$  BafA1 for 1 h at 37°C. This assay was performed as described previously<sup>70</sup>.

HEK293T cells ( $4 \times 10^6$ ) were plated in 10-cm plates. The next day, the medium was replaced with medium containing 2.2 mg ml<sup>-1</sup> FITC-Dextran (Millipore Sigma FD40), to allow uptake of the dye by endocytosis. The following day, FITC-Dextran-containing medium was replaced with regular unlabeled medium that permits all dye to progress to the lysosomal compartment<sup>71</sup>. Cells were either left untreated (DMSO control) or treated with 15  $\mu\text{M}$  249C or 0.5  $\mu\text{M}$  BafA1 for 1 h at 37°C. After treatment, cells were placed on ice, rinsed with ice-cold PBS and collected by scraping into fractionation buffer (125 mM KCl, 1 mM ethylenediaminetetraacetic acid, 50 mM sucrose, 20 mM HEPES, 1 mM PMSF, and Halt protease inhibitors). Cells were collected by centrifugation at 1,200g for 5 min, resuspended in fractionation buffer and lysed by passing through a 27-gauge needle 10 times. Cell lysates were cleared of nuclei and intact cells by centrifugation at 2,000g for 10 min and the resulting supernatant was then centrifuged again for 15 min at 16,100g to sediment the FITC-Dextran-containing lysosomes<sup>72,73</sup>. The resulting pellets were resuspended in 100  $\mu\text{l}$  of fractionation buffer and subjected to a Bradford assay to assess protein concentration<sup>74</sup>. To measure molecule-dependent proton pumping, 20  $\mu\text{g}$  protein was added to fractionation buffer pre-warmed to 37°C. Sample fluorescence was excited at 490 nm, and emission fluorescence at 520 nm was measured continuously in BioTek plate reader (Synergy) using Gen5 software (v.3.05). After initial fluorescence stabilization, 1 mM ATP and 2 mM MgCl<sub>2</sub> were added to initiate ATPase activity and proton pumping into the lysosomes, which causes quenching of FITC in the lysosomal lumen. The V-ATPase dependence of quenching was verified by adding 249C and BafA1, which inhibit fluorescence quenching. Representative of five individual experiments with  $n = 2$  for each is presented. MEFs were processes in a similar way.

**Proton pumping assay in yeast.** Spheroplasts from wild-type yeast (a gift from the Walter lab at UCSF) were left untreated (DMSO control) or treated with 29  $\mu\text{M}$  249C, or 1  $\mu\text{M}$  BafA1 for 2.5 h with shaking at 30°C and vacuolar membrane vesicles were isolated as previously described<sup>75</sup>. Proton transport was measured using ATP-dependent quenching of 9-amino-6-chloro-2-methoxy-acridine (Acridine Orange, Thermo Fisher) fluorescence quenching for isolated vacuoles as previously described<sup>76</sup>.

**Biochemical V-ATPase assay.** V-ATPase was purified as described previously from yeast<sup>77</sup> using the detergent dodecylmaltoside and porcine kidney<sup>78</sup> using the detergent glycol-diosgenin. ATPase assays with purified V-ATPase were performed as described previously. 249C (mammalian: 0.1, 1, 10, 100  $\mu\text{M}$ ; and yeast: 5, 10 and 100  $\mu\text{M}$ ) or BafA1 (1  $\mu\text{M}$ ) were added to the reaction and compared with a negative control to which only DMSO was added. Enzyme-coupled ATPase biochemical activity assays were performed in a 96-well plate as described previously<sup>79</sup>.

### Three-dimensional molecular modeling, binding pocket detection and docking.

A preliminary sequence alignment between the yeast (Uniprot P41807) and human (Uniprot Q9UI12) sequences, which share 27% homology/45% similarity, was generated with EMBOSS Stretcher on EMBL-EBI webserver. The alignment was then manually adjusted to avoid alignment gaps within secondary structural elements of the human protein, as predicted by the DISSPRED webserver (<https://comp.chem.nottingham.ac.uk/disspred/>). Next the human V-type proton ATPase, encoded by ATP6VIH was modeled on the basis of the yeast homolog structure available in the PDB database (PDB ID 1HO8) using the MODELLER<sup>80</sup> software v.9.19. The best model on the basis of the DOPE<sup>81</sup> score was used for subsequent virtual screening.

The Small Molecule Drug Discovery Suite 2019-1<sup>82</sup> (Schrödinger) was used for binding pocket detection and virtual screening. The protein was prepared in a ready-to-dock-format with the Protein Preparation Wizard workflow. The hydroxyl group orientations and protonation states were assigned at pH 7 using PROPKA in Epik v.4.7. The SiteMap algorithm was used to screen for potential binding pockets within the entire surface of the protein pocket, using standard parameters. Small molecules were drawn with Maestro v.11.9, and their protonation states and tautomers assigned at pH 7.0  $\pm$  2 in Epik v.4.7. Conformers were assigned using LigPrep v.4.9 with the OPLS3e force field. Next, Glide v.8.2 was used to generate a grid box for docking the small molecules into each detected binding site. Before docking, a 37  $\times$  37  $\times$  37 Å (ref. <sup>82</sup>) docking grid was erected. The Glide XP<sup>83</sup> scoring function was employed, and the strain energy was included in the final docking score, a maximum of ten docking poses was set for each ligand. Planarity of aromatic groups was enforced. Final binding poses were picked on the basis of a combination of visual inspection, chemical intuition, and score.

### Macropinosome visualization and quantification.

Macropinosome visualization was essentially done as previously described<sup>84</sup>. Cells were plated in black, clear bottom CellCarrier-96 Ultra Microplates (Perkin Elmer 6055302) and serum-starved for 24 h. The next day, they were treated with 2  $\mu\text{M}$  249C (1255) for 18 h followed by addition of 70 kDa tetramethylrhodamine (TMR)–Dextran (Invitrogen D1818) and Hoescht for 2 h at 37°C followed by 3× cold PBS washes and fixation in 4% paraformaldehyde for 30 min. Following 3× cold PBS washes,

mounting medium (Vector Laboratories) was added and images were captured using an Operetta CLS fluorescent microscope for High-Content Analysis (Perkin Elmer). Image analysis and quantification was performed with a spot segmentation algorithm using the Perkin Elmer Harmony PhenoLOGIC 3.2 software. In brief, the images were segmented and individual nuclei (DAPI stained) and cell bodies (by digital phase contrast imaging) were identified. The TMR signal was used for the spot segmentation analysis block. Number of spots, area, and TMR fluorescence intensity were calculated for each cell region, and displayed as mean values per cell. Data are presented as spots – number of objects per nucleus. For each cell line, five DMSO control and five 249C-treated wells were imaged and a minimum of three images were captured per well. Data representing three independent experiments are presented.

**Immunofluorescence assays.** Cells were seeded onto glass coverslips and subsequently serum-starved for 24 h. After serum starvation, cells were treated with 500 nM 249C for ~15 h and fixed with 4% formaldehyde for 30 min at room temperature. The following sequential steps took place at room temperature: cells were washed twice with PBS, permeabilized (0.1% Tween in PBS) for 10 min, and blocked (5% bovine serum in PBS) for 30 min. The following primary antibodies were used: ATP6V<sub>1</sub>A (Abnova, H0000523-M02 1:250 dilution), ATP6V<sub>1</sub>B2 (Thermo Fisher, PA552518, 1:50 dilution), ATP6V<sub>1</sub>H (PA552518, Fisher, 1:50 dilution), EGFR (4267P, Cell Signaling, 1:100 dilution). Corresponding AlexaFluor-488 secondary antibodies were used at 1:500 dilution (Thermo Fisher, mouse: A11001, rabbit: A11008). Cells were mounted onto slides using Mounting Media (Vector Laboratories) containing DAPI. A minimum of three images per well were captured using a spinning disk confocal microscope (Zeiss with ZEN blue software (2012)). Data representing two independent experiments are presented.

**Plasma membrane fractionation.** The plasma membrane protein extraction kit (BioVision, K268-50) was used to separate the plasma membrane fraction from other cellular membranes according to the manufacturer's recommended protocol. Data representing two independent experiments are presented.

**Apoptosis assays.** Cells were treated with 100 nM 249C for 48 h and following two washes with ice-cold PBS, they were stained using a FITC Annexin V/PI Apoptosis Detection kit (BD Pharmingen) following the manufacturer's recommendations. Samples were analyzed by flow cytometry on a BD LSR II flow cytometer with FACSDiva software (v.8.0). Gating strategy: preliminary forward scatter/side scatter (FSC/SSC) gates were applied followed by removal of doublets (FSC-H versus FSC-A and also SSC-H versus SSC-A). Next, single-color controls (FITC only or PI only) and double-positive controls (FITC<sup>+</sup> and PI<sup>+</sup>) were run to set gates for the double-positive population. Finally, untreated and 249C-treated samples were run keeping these gates constant for all.

**Animal studies, plasma concentration, body weight.** A549 cells ( $5 \times 10^6$ ) were subcutaneously injected into the lower left flank of 6–8-week old athymic nude female mice (Charles River strain 088, homozygous NU/NU). To assess establishment of tumors, mice were examined 5 days after inoculation and were randomly segregated into two treatment groups (vehicle control, 10 mg kg<sup>-1</sup> 249C i.p.,  $n = 7$  per group) and were treated twice daily with the drug in N-methyl-2-pyrrolidone (NPM) or vehicle control (5% weight aqueous solution of carboxymethyl cellulose). Tumor volumes were calculated using the formula (length  $\times$  width  $\times$  height)/2 with recorded caliper measurements. Survival curves and statistical analyses were performed using Excel. Animals were maintained on a standard chow diet; 12h/12h dark/light cycle and in group housing in HEPA-filtered cages. All animal procedures were performed under IACUC-approved protocols and guidelines. Animals from both groups were weighed every 3 days. Plasma concentration was measured from blood collected using standard and established protocols.

For cell line xenografts,  $6 \times 10^6$  SW48 cells were subcutaneously injected into the flanks of 6–8-week old athymic nude female mice (Taconic model NCRNU-F, CrTac:NCR-Foxn1 sp/sp) and tumor growth was monitored with caliper measurement. Once the mean tumor reached a certain volume (between 100–200 mm<sup>3</sup>), animals were randomized into different treatment groups of five animals per group. 249C for in vivo use was formulated in 0.5% methylcellulose and dosed i.p. (10 mg kg<sup>-1</sup>, for 2 weeks). Antitumor activity was determined by calculating the treatment over control tumor volume ratio at the end of the study. Either at the end of each study, or if any animal reached a humane end point, animals were killed with CO<sub>2</sub> followed by cervical dislocation or another secondary method of killing approved by the IACUC protocol. Mouse manipulations were performed in accordance with UCSF's IACUC protocol AN179973. Mice were housed in the UCSF Animal Care Facility LARC at the Helen Diller Family Cancer Center at UCSF Mission Bay. Mice were housed in a specific-pathogen-free individual suite. They are housed up to five per cage in ventilator cages, with ad libitum food and water on a 12-h light cycle and controlled temperature and humidity conditions (67–74 °F and 30–70%).

**Ex vivo analysis.** At the end point, tumors were harvested, weighed and minced up. Total protein from frozen tissues was prepared with T-PER (Thermo Fisher Scientific) supplemented with protease and phosphatase inhibitors (Roche). Equal

quantities of proteins were combined with 5 $\times$  protein loading buffer and separated by SDS-PAGE followed by PVDF membrane transfer. Membranes were blocked with 5% milk followed by incubation with LC3 (Cell Signaling) and GAPDH (Thermo Fisher) antibodies. Blots were developed with ECL Reagents (Pierce).

**Maximum tolerated dose Studies.** Maximum tolerated dose studies were outsourced and performed at a local contract research organization (CRO) on the basis of their established protocols.

**hERG assay.** The fluorescence polarization-based assay to characterize the affinity of 249C for hERG responsible for electrical activity of the heart was performed as previously described<sup>85</sup>.

**BioMAP.** The BioMAP Toxicity Screening Profile was performed as described previously<sup>86</sup>.

**Kinome scan.** The KINOMEScan Profiling Service consisting of 468 human kinases was used to assess 249C inhibitor activity to check for off-target effects as previously described<sup>87</sup>.

**Lactate dehydrogenase assay.** Cells were left untreated (DMSO) or treated with indicated concentrations of 249C, 68, 148D, and 226 C for 48 h. The lactate dehydrogenase (LDH) cytotoxicity assays were performed using a kit (Pierce 88953) and following the manufacturer's recommendations.

**Statistical analyses.** All experiments were repeated a minimum of two times with at least duplicate or triplicate samples and measurements were taken from distinct samples. Values including controls are expressed as the mean  $\pm$  s.d. or mean  $\pm$  s.e.m. Two-tailed paired Student's *t*-test was used to test for differences between two groups unless indicated otherwise. Differences with a  $P \leq 0.05$  were considered as statistically significant.

**Reporting summary.** Further information on research design is available in the Nature Research Reporting Summary linked to this article.

## Data availability

Datasets that support the findings of this study are available in the Source Data, Supplementary Figs 1–19 and Supplementary Tables 1–6. Mutation analysis in CCLE cell lines: the Combined Annotation Dependent Database (<https://cadd.gs.washington.edu/>) was used to assess the predicted functional importance of SNVs (v.1.6). Cell line mutation data (CCLE\_DepMap\_18q3\_maf\_20180718.txt) were downloaded from the CCLE at <https://depmap.org/portal/download/> (2018). Mass spectrometry Gene Ontology gene sets: GSEA (v.4.2.3) software and Molecular Signature Database (MSigDB v.7.4) from <https://www.gsea-msigdb.org/gsea/index.jsp> was used to query the top proteins from the Whole Proteome Analysis for Gene Ontology gene sets in NCI-60 cell lines. CRISPR screen: sgRNA read counts and phenotypes for all pooled screens are provided as supplementary tables. All other data will be made available by the corresponding author upon request. Source data are provided with this paper.

## Code availability

Scripts for CRISPR screen analysis used in this manuscript build on previously published scripts. The Python-based ScreenProcessing pipeline is available at <https://github.com/mhorbeck/ScreenProcessing><sup>25</sup>. All custom scripts will be made available upon request.

## References

- Barretina, J. et al. The Cancer Cell Line Encyclopedia enables predictive modelling of anticancer drug sensitivity. *Nature* **483**, 603–607 (2012).
- Kircher, M. et al. A general framework for estimating the relative pathogenicity of human genetic variants. *Nat. Genet.* **46**, 310–315 (2014).
- Ting, L., Rad, R., Gygi, S. P. & Haas, W. MS3 eliminates ratio distortion in isobaric multiplexed quantitative proteomics. *Nat. Methods* **8**, 937–940 (2011). Oct 2.
- McAlister, G. C. et al. MultiNotch MS3 enables accurate, sensitive, and multiplexed detection of differential expression across cancer cell line proteomes. *Anal. Chem.* **86**, 7150–7158 (2014).
- Subramanian, T. et al. Gene set enrichment analysis: a knowledge-based approach for interpreting genome-wide expression profiles. *Proc. Natl Acad. Sci. USA* **102**, 15545–15550 (2005).
- Liberzon, A. et al. The Molecular Signatures Database (MSigDB) hallmark gene set collection. *Cell Syst.* **1**, 417–425 (2015).
- Kunkel, E. J. et al. Rapid structure–activity and selectivity analysis of kinase inhibitors by BioMAP analysis in complex human primary cell-based models. *Assay Drug Dev. Technol.* **2**, 431–441 (2004).
- Berg, E. L., Yang, J. & Polokoff, M. A. Building predictive models for mechanism-of-action classification from phenotypic assay data sets. *J. Biomol. Screen.* **18**, 1260–1269 (2013).

65. Kingsley, R. E. & Cole, N. L. Preparation of cultured mammalian cells for transmission and scanning electron microscopy using ACLAR® film. *J. Electron Microsc. Tech.* **10**, 77–85 (1988).
66. Sato, T. A modified method for lead staining of thin sections. *J. Electron Microsc. Tech.* **17**, 158–159 (1968).
67. Gilbert, L. A. et al. Genome-scale CRISPR-mediated control of gene repression and activation. *Cell* **159**, 647–661 (2014).
68. Jost, M. et al. Titrating gene expression using libraries of systematically attenuated CRISPR guide RNAs. *Nat. Biotechnol.* **38**, 355–364 (2020).
69. Kampmann, M., Bassik, M. C. & Weissman, J. S. Integrated platform for genome-wide screening and construction of high-density genetic interaction maps in mammalian cells. *Proc. Natl Acad. Sci. USA* **110**, E2317–E2326 (2013).
70. Stransky, L. A. & Forgac, M. Amino acid availability modulates vacuolar H<sup>+</sup>-ATPase assembly. *J. Biol. Chem.* **290**, 27360–27369 (2015).
71. Galloway, C. J., Dean, G. E., Marsh, M., Rudnick, G. & Mellman, I. Acidification of macrophage and fibroblast endocytic vesicles in vitro. *Proc. Natl Acad. Sci. USA* **80**, 3334–3338 (1983).
72. Steinberg, B. E. et al. A cation counterflux supports lysosomal acidification. *J. Cell Biol.* **189**, 1171–1186 (2010).
73. Zoncu, R. et al. mTORC1 senses lysosomal amino acids through an inside-out mechanism that requires the vacuolar H<sup>+</sup>-ATPase. *Science* **334**, 678–683 (2011).
74. Lowry, O. H., Rosebrough, N. J., Farr, A. L. & Randall, R. J. Protein measurement with the Folin phenol reagent. *J. Biol. Chem.* **193**, 265–275 (1951).
75. Roberts, C. J., Raymond, C. K., Yamashiro, C. T. & Stevens, T. H. Methods for studying the yeast vacuole. *Methods Enzymol.* **194**, 644–661 (1991).
76. Feng, Y. & Forgac, M. A novel mechanism for regulation of vacuolar acidification. *J. Biol. Chem.* **267**, 5817–5822 (1992).
77. Benlekbir, S., Bueler, S. A. & Rubinstein, J. L. Structure of the vacuolar-type ATPase from *Saccharomyces cerevisiae* at 11-Å resolution. *Nat. Struct. Mol. Biol.* **19**, 1356–1362 (2012).
78. Abbas, Y. M., Wu, D., Bueler, S. A., Robinson, C. V. & Rubinstein, J. L. Structure of V-ATPase from the mammalian brain. *Science* **367**, 1240–1246 (2020).
79. Vasanthakumar, T. et al. Structural comparison of the vacuolar and Golgi V-ATPases from *Saccharomyces cerevisiae*. *Proc. Natl Acad. Sci. USA* **116**, 7272–7277 (2019).
80. & Eswar, N. et al. Comparative protein structure modeling using Modeller. *Curr. Protoc. Bioinform.* **15**, 5.6.1–5.6.30 (2006).
81. Shen, M. Y. & Sali, A. Statistical potential for assessment and prediction of protein structures. *Protein Sci.* **15**, 2507–2524 (2006).
82. Schrödinger Release 2019-1 (Schrödinger LLC, 2019).
83. Friesner, R. A. et al. Extra precision glide: docking and scoring incorporating a model of hydrophobic enclosure for protein–ligand complexes. *J. Med. Chem.* **49**, 6177–6196 (2006).
84. Commisso, C., Flinn, R. J. & Bar-Sagi, D. Determining the macropinocytic index of cells through a quantitative image-based assay. *Nat. Protoc.* **9**, 182–192 (2014).
85. Piper, D. R. et al. Development of the predictor HERG fluorescence polarization assay using a membrane protein enrichment approach. *Assay Drug Dev Technol.* **6**, 213–223 (2008).
86. Kleinstreuer, N. C. et al. Phenotypic screening of the ToxCast chemical library to classify toxic and therapeutic mechanisms. *Nat. Biotechnol.* **32**, 583–591 (2014).
87. Davis, M. et al. Comprehensive analysis of kinase inhibitor selectivity. *Nat. Biotechnol.* **29**, 1046–1051 (2011).

## Acknowledgements

This study was supported in part by the UCSF Helen Diller Family Comprehensive Cancer Center Laboratory for Cell Analysis Shared Resource Facility through a grant from NIH (P30CA082103). All microscopy data was collected at the Lab for Cell Analysis. Flow Cytometry was performed at the UCSF Parnassus Flow Core facility (RRID: SCR\_018206), which is supported in part by the NIH DRC Center Grant (P30 DK063720). The whole proteome mass spectrometry was performed at the Thermo Fisher Scientific Center for Multiplexed Proteomics. We thank several CROs for screening our molecule in targeted assays for a fee. The authors thank the following individuals for their generous contributions: H. Goodarzi at UCSF (MDA-MB-231 CRISPRi cells) and D. Brown at Harvard University (ATP6V<sub>1</sub>A and ATP6V<sub>1</sub>B2

antibodies used for Fig. 3). The MEF cells expressing human *KRAS* or *BRAF* were from the Frederick National Laboratory for Cancer Research, National Cancer Institute. We thank K. Yamamoto and J. Debnath from UCSF for valuable discussions. We thank M. Forgac and S. Wilkens for technical discussions. We thank L. Acevedo and N. Hoang for assistance with Western blotting. We thank M. Boone from the Walter lab at UCSF for yeast and related reagents. We thank the Wells lab at UCSF for use of the Octet RED384 for binding studies. We thank the Chief of the UCSF Thoracic Oncology laboratory for lab space and staff chemists for assistance with chemical synthesis/reagents. We thank P. Derish, UCSF Department of Surgery, for editorial assistance. Fig. 4 was created with BioRender (<https://biorender.com>). This work was supported by a UCSF Pancreas Center Pilot Project Grant Award funded by the Bern Schwartz Family Foundation (MMEPHMT603 to B.T.), the UCSF Hellman Family Award for Early Career Faculty (12RBP0002 to B.T.), the UCSF Thoracic Oncology Program laboratory (B.T.), the Canadian Institutes of Health Research postdoctoral fellowship (CIHR-IRSC:0525009424 to Y.Z.T.), an Ontario Graduate Scholarship (T.V.), the American Heart Association Postdoctoral Fellowship (18POST33960587 to P.B.), the Canada Research Chairs program and Canadian Institutes of Health Research grant (PJT166152 to J.L.R.), the National Institutes of Health (K99 GM130964 and R00 GM130964 to M.J. and 1RM1 HG009490-01 to J.S.W.). J.S.W. is a Howard Hughes Medical Institute Investigator.

## Author contributions

Conception and design: B.T., M.J., J.S.W. Funding support and acquisition: B.T., J.S.W. Preparation of the manuscript: B.T., M.J., J.S.W. All other authors provided feedback. Analyses and interpretation of data: B.T., A.C., Y.Z.T., R.F., A.J.S., T.V., J.L.R., M.J., J.S.W. M.J. analyzed and interpreted CRISPRi data. Acquisition of data: B.T. screened ~300 molecules via cellular assays, calculated IC<sub>50</sub> values, screened 249C in 53 cancer cell lines, prepared samples for whole proteome mass spec, oversaw comparative profiling, performed immunoblotting, performed LysoSensor and LysoTracker experiments. B.T. performed the CRISPRi screen and individual re-tests with guidance from M.J. and J.S.W. B.T. performed subcellular fractionation, mammalian proton pumping assays, yeast proton pumping assays, assisted with H subunit protein purification, and performed Octet/BLI binding studies. B.T. performed cellular assays in MEFs, MP assays with dextran, immunofluorescence staining, plasma membrane isolation, and ex vivo analysis. B.T. performed the LDH cytotoxicity assay and oversaw the remainder of assays. A.C. captured microscopy images and assisted in MP high-content analysis. Y.Y. and I.B.S. performed and supported chemical synthesis, respectively. A.D.C. performed spectral analyses for compounds. Y.Z.T. purified mammalian V-ATPase used for Octet/BLI studies, performed mammalian V-ATPase assays, and analyzed the data. R.F. performed electron microscopy and analyzed data. A.J.S. performed statistical analysis for WT and mutant IC<sub>50</sub> values using CCLE. T.V. performed yeast V-ATPase assays and analyzed data. P.B. performed 3D docking. C.R.L. isolated DNA for next-generation sequencing for CRISPRi. M.J. provided extensive technical expertise on CRISPRi screening.

## Competing interests

B.T. is an inventor on the patent filed by UCSF covering these molecules. UCSF has licensed this patent to a start-up biotechnology company. The startup calls 249C 'RSC-1255' instead and is running a Phase Ia/Ib dose escalation and dose expansion clinical trial for the following indications: Ras mutations; lung cancer; colon cancer; pancreatic cancer; and glioblastoma. It is being run as a multi-center trial across five different sites in the U.S. Recruitment is ongoing (NCT04678648). J.S.W. and M.J. have submitted patent applications related to CRISPR screening. J.S.W. declares outside interest in 5 AM Venture, Amgen, Chroma Medicine, DEM Biosciences, KSQ Therapeutics, Maze Therapeutics, Tenaya Therapeutics, Tessera Therapeutics and Velia Therapeutics. M.J. consults for Maze Therapeutics and Gate Biosciences. All other authors declare no competing interests.

## Additional information

**Supplementary information** The online version contains supplementary material available at <https://doi.org/10.1038/s41587-022-01386-z>.

**Correspondence and requests for materials** should be addressed to Bhairavi Tolani or Marco Jost.

**Peer review information** *Nature Biotechnology* thanks Alessandra d'Azzo, Kirsten Bryant, Philippe Cassier and the other, anonymous, reviewer(s) for their contribution to the peer review of this work.

**Reprints and permissions information** is available at [www.nature.com/reprints](http://www.nature.com/reprints).

## Reporting Summary

Nature Portfolio wishes to improve the reproducibility of the work that we publish. This form provides structure for consistency and transparency in reporting. For further information on Nature Portfolio policies, see our [Editorial Policies](#) and the [Editorial Policy Checklist](#).

### Statistics

For all statistical analyses, confirm that the following items are present in the figure legend, table legend, main text, or Methods section.

- | n/a                                 | Confirmed  |
|-------------------------------------|--|
| <input type="checkbox"/>            | <input checked="" type="checkbox"/> The exact sample size ( $n$ ) for each experimental group/condition, given as a discrete number and unit of measurement  |
| <input type="checkbox"/>            | <input checked="" type="checkbox"/> A statement on whether measurements were taken from distinct samples or whether the same sample was measured repeatedly  |
| <input type="checkbox"/>            | <input checked="" type="checkbox"/> The statistical test(s) used AND whether they are one- or two-sided<br><i>Only common tests should be described solely by name; describe more complex techniques in the Methods section.</i>   |
| <input checked="" type="checkbox"/> | <input type="checkbox"/> A description of all covariates tested  |
| <input checked="" type="checkbox"/> | <input type="checkbox"/> A description of any assumptions or corrections, such as tests of normality and adjustment for multiple comparisons   |
| <input type="checkbox"/>            | <input checked="" type="checkbox"/> A full description of the statistical parameters including central tendency (e.g. means) or other basic estimates (e.g. regression coefficient) AND variation (e.g. standard deviation) or associated estimates of uncertainty (e.g. confidence intervals) |
| <input type="checkbox"/>            | <input checked="" type="checkbox"/> For null hypothesis testing, the test statistic (e.g. $F$ , $t$ , $r$ ) with confidence intervals, effect sizes, degrees of freedom and $P$ value noted<br><i>Give <math>P</math> values as exact values whenever suitable.</i>                            |
| <input checked="" type="checkbox"/> | <input type="checkbox"/> For Bayesian analysis, information on the choice of priors and Markov chain Monte Carlo settings  |
| <input checked="" type="checkbox"/> | <input type="checkbox"/> For hierarchical and complex designs, identification of the appropriate level for tests and full reporting of outcomes  |
| <input type="checkbox"/>            | <input checked="" type="checkbox"/> Estimates of effect sizes (e.g. Cohen's $d$ , Pearson's $r$ ), indicating how they were calculated   |

*Our web collection on [statistics for biologists](#) contains articles on many of the points above.*

### Software and code

Policy information about [availability of computer code](#)

#### Data collection

Cell Proliferation Assays: Data was collected using Promega's GLOMAX software (version 1.9.3)

Mutation Analysis in CCLE Cell Lines: Data from cell proliferation assays were used

Electron Microscopy: images were collected using Gatan Microscopy Suite DigitalMicrograph (version 3.4.3) and SerialEM (version 3.8.6)

Fluorescence Microscopy (LysoTracker, LysoSensor, ATP6V staining): Data was collected using ZEN blue from Carl Zeiss (2012)

CRISPR Screen: Next-generation sequencing data were collected using commercially available software from Illumina (HiSeq Software Suite v3.4.0)

Flow Cytometry: Data was collected FACSDiva software (version 8.0)

Proton Pumping: fluorescence data was collected using Gen5 (version 3.05) software from BioTek

Bio-Layer Interferometry Studies: Octet R software (version 12) was used for data collection

Macropinosome Visualization: Data were captured using Perkin Elmer Harmony® PhenoLOGIC™ software (version 3.2)

The following data were collected externally for a fee: Whole Proteome Mass Spectrometry, comparative profiling in a panel of primary cell-based systems, hERG activity, BioMAP Screening, in vivo plasma concentration, and the KINOMEScan™ screening.

#### Data analysis

Cell Proliferation Assays: Data was analyzed using Excel (2016) and GraphPad Prism (version 6)



Mutation Analysis in CCLE Cell Lines: Statistical analyses were performed in R (version 3.6.3). Multiple two-sided Wilcoxon rank sum tests were performed in R using the "wilcox.test" and "lapply" functions. The Combined Annotation Dependent Database (<https://cadd.gs.washington.edu/>) was used to assess the predicted functional importance of SNVs (version 1.6). Cell line mutation data (CCLE\_DepMap\_18q3\_maf\_20180718.txt) were downloaded from the Cancer Cell Line Encyclopedia (CCLE) at <https://depmap.org/portal/download/> (2018).

Whole Proteome Analysis: GSEA software (version 4.2.3) and Molecular Signature Database (MSigDB version 7.4)

Electron Microscopy: images were montaged using TrakEM2 within Fiji (ImageJ version 1.53c). The montages were analyzed using IMOD (version 4.12.3). Data was analyzed with Excel and GraphPad Prism

Fluorescence Microscopy: No analyses were performed

CRISPR Screen: Sequencing reads from pooled CRISPR screens were aligned to the library sequences, counted, and quantified using the Python-based ScreenProcessing pipeline (<https://github.com/mhorlbeck/ScreenProcessing>). All analyses of screen data were performed in python3.7 using custom code based on Numpy (v1.15.4), Pandas (v0.25.3), and Scipy (v1.4.1). The p-values are derived from a two-sided Mann-Whitney U-test.

Flow Cytometry: Data was analyzed using Excel (2016)

Biochemical V-ATPase Assay and Proton Pumping: Commercially available software was used (Excel 2016 and GraphPad Prism v6)

Bio-Layer Interferometry Studies: Octet R software (version 12) was used for data analysis

Macropinosome Visualization: Data were analyzed using Perkin Elmer Harmony® PhenoLOGIC™ software (version 3.2)

3D Molecular Modeling, Binding Pocket Detection and Docking: All the software used is commercially available and described in the Methods section (EMBOSS Stretcher on EMBL-EBI webserver, DISSPRED webserver, MODELLER25 version 9.19, DOPE, Small Molecule Drug Discovery Suite 2019-127 (Schrödinger, LLC), SiteMap algorithm, Maestro v11.9, LigPrep v4.9, and Glide v.8.2)

The following data were analyzed externally: Whole Proteome Mass Spectrometry, comparative profiling in a panel of primary cell-based systems, hERG activity, BioMAP Screening, in vivo plasma concentration, and the KINOMEscan™ screening.

For manuscripts utilizing custom algorithms or software that are central to the research but not yet described in published literature, software must be made available to editors and reviewers. We strongly encourage code deposition in a community repository (e.g. GitHub). See the Nature Portfolio [guidelines for submitting code & software](#) for further information.

## Data

Policy information about [availability of data](#)

All manuscripts must include a [data availability statement](#). This statement should provide the following information, where applicable:

- Accession codes, unique identifiers, or web links for publicly available datasets
- A description of any restrictions on data availability
- For clinical datasets or third party data, please ensure that the statement adheres to our [policy](#)

Datasets that support the findings of this study are available in Source Data/Supplementary Figures and Tables.

Mutation Analysis in CCLE Cell Lines: The Combined Annotation Dependent Database (<https://cadd.gs.washington.edu/>) was used to assess the predicted functional importance of SNVs (version 1.6). Cell line mutation data (CCLE\_DepMap\_18q3\_maf\_20180718.txt) were downloaded from the Cancer Cell Line Encyclopedia (CCLE) at <https://depmap.org/portal/download/> (2018).

Mass Spectrometry GO gene sets: GSEA (version 4.2.3) software and Molecular Signature Database (MSigDB version 7.4) from <http://www.broad.mit.edu/gsea> was used to query the top proteins from the Whole Proteome Analysis for GO gene sets in NCI-60 cell lines

CRISPR Screen: sgRNA read counts and phenotypes for all pooled screens are provided as supplementary tables

## Field-specific reporting

Please select the one below that is the best fit for your research. If you are not sure, read the appropriate sections before making your selection.

Life sciences  Behavioural & social sciences  Ecological, evolutionary & environmental sciences

For a reference copy of the document with all sections, see [nature.com/documents/nr-reporting-summary-flat.pdf](https://www.nature.com/documents/nr-reporting-summary-flat.pdf)

## Life sciences study design

All studies must disclose on these points even when the disclosure is negative.

Sample size

For all experiments, no sample size calculation was performed. Sample sizes were chosen empirically based on previously published work, knowledge of intra-group variation and expected effect sizes, or based on discussions with experts in their respective fields. These sample sizes were sufficient for statistical analysis.

Cell Proliferation Assays: Each compound OR cell line was tested a minimum of 2 times with n = 3

Mutation Analysis in CCLE Cell Lines: We analyzed mutations in the 53 cell lines that were also included in our MTS assays

Electron Microscopy: Images were taken from single replicate samples for each condition. A minimum of 10 cells for each sample were randomly imaged and measured for the scored parameters. For some structures, up to a total of 100 measurements were from the minimum of 10 cells for each condition.

CRISPR Screen: No sample size calculation was performed. The pooled genetic screen was performed as a single replicate. Each gene was targeted with 5 independent sgRNAs, providing internal replicates. Individual hits were validated in duplicate or triplicate in individual re-tests.

Flow Cytometry: Experiments were performed in duplicates at least

Biochemical V-ATPase Assay and Proton Pumping: at minimum, each bar represents mean +/- SD, n=3

Bio-Layer Interferometry Studies: Two individual experiments were performed

Macropinosome Visualization: For each cell line, 5 DMSO control and 5 249C-treated wells were imaged and a minimum of 3 images were captured per well

Animal Studies: sample size was decided based on discussions with the UCSF animal core facility

Data exclusions	<p>CRISPR Screen: For the pooled screens, we required that sgRNAs had &gt;49 counts in at least one of the two conditions that was being compared to calculate a given phenotype (pre-established exclusion criterion).</p> <p>For all other experiments, no data were excluded.</p>
Replication	<p>All experiments were performed in duplicate or triplicate unless otherwise stated. All attempts at replication were successful. For the CRISPR screens, selected hits were replicated in duplicate or triplicate. For the electron microscopy, a minimum of 10 cells was captured for each sample in a single experiment. The biochemical V-ATPase assay was performed twice from one enzymatic preparation due to limitations on bovine tissue acquisition. Animal studies were performed once with 5 mice per treatment group housed separately.</p>
Randomization	<p>Animal Studies: Once the mean tumor reached a certain volume (between 100-200 mm<sup>3</sup>), animals were randomized into different treatment groups.</p> <p>For all other experiments, cells or samples were randomly assigned to control or treatment groups.</p>
Blinding	<p>Electron Microscopy: The individuals who collected and analyzed data was blinded to group allocation during data collection and for data analysis.</p> <p>Macropinosome Visualization: Fields of view were randomly selected using the Harmony software prior to automated imaging of the whole plate to ensure unbiased image acquisition and individuals who collected data were blinded to group allocation during data analysis.</p> <p>Animal Studies: Individuals who performed the SW48 xenograft experiments were blinded to group allocation during data collection and for data analysis.</p> <p>For all other experiments, blinding is not applicable as the quantitative analyses performed are not subject to human bias</p>

## Reporting for specific materials, systems and methods

We require information from authors about some types of materials, experimental systems and methods used in many studies. Here, indicate whether each material, system or method listed is relevant to your study. If you are not sure if a list item applies to your research, read the appropriate section before selecting a response.

### Materials & experimental systems

n/a	Involvement in the study
<input type="checkbox"/>	<input checked="" type="checkbox"/> Antibodies
<input type="checkbox"/>	<input checked="" type="checkbox"/> Eukaryotic cell lines
<input checked="" type="checkbox"/>	<input type="checkbox"/> Palaeontology and archaeology
<input type="checkbox"/>	<input checked="" type="checkbox"/> Animals and other organisms
<input checked="" type="checkbox"/>	<input type="checkbox"/> Human research participants
<input checked="" type="checkbox"/>	<input type="checkbox"/> Clinical data
<input checked="" type="checkbox"/>	<input type="checkbox"/> Dual use research of concern

### Methods

n/a	Involvement in the study
<input checked="" type="checkbox"/>	<input type="checkbox"/> ChIP-seq
<input type="checkbox"/>	<input checked="" type="checkbox"/> Flow cytometry
<input checked="" type="checkbox"/>	<input type="checkbox"/> MRI-based neuroimaging

## Antibodies

Antibodies used

- 1) SQSTM1 (Cell Signaling: 8025, D5E2, Lot: 5)
- 2) LC3A/B (Cell Signaling: 12741T, (D3U4C) XP®, Lot: 4)

- 3) GAPDH (ThermoFisher: AM4300, 6C5, lot: 00439919)
- 4) ATP6V1B2 (ThermoFisher: PA5-52518, No clone#, lot: VJ3104174) + Received from Dr. Dennis Brown
- 5) ATP6V0D1/P39 (Abcam: ab56441, 2G12, lot: GR3299463-l)
- 6) ATP6V1H (Fisher: PIPA554793, No clone#, lot: UL289506)
- 7) ATP6V1A (Abnova: H00000523-M02, 4F5, lot: K5261) + Received from Dr. Dennis Brown
- 8) RAS (Cell Signaling: 3965, No clone#, lot: 4)
- 9) EGFR (Cell Signaling: 4267, No clone#, lot: 24)
- 10) Alexa-Fluor 488 goat anti-mouse IgG (ThermoFisher: A11001, No clone#, lot: 745480)
- 11) Alexa-Fluor 488 goat anti-rabbit IgG (ThermoFisher: A11008, No clone#, lot: 2179202)

## Validation

All vendors showed validation data for antibodies on their websites (including Western blot, IF, IHC etc.)

## Manufacturer's Website:

- 1) SQSTM1 (Cited in 195 publications: <https://www.cellsignal.com/products/primary-antibodies/sqstm1-p62-d5e2-rabbit-mab/8025?site-search-type=Products&N=4294956287&Ntt=8025st&fromPage=plp>)
- 2) LC3A/B (Cited in 521 publications: <https://www.cellsignal.com/products/primary-antibodies/lc3a-b-d3u4c-xp-rabbit-mab/12741>)
- 3) GAPDH (Cited in 474 publications: <https://www.thermofisher.com/antibody/product/GAPDH-Antibody-clone-6C5-Monoclonal/AM4300>)
- 4) ATP6V1B2 (Citations not listed; testing methodology provided: <https://assets.thermofisher.com/TFS-Assets/LSG/Flyers/commitment-antibody-performance-flyer.pdf>; validation provided on website: <https://www.thermofisher.com/antibody/product/ATP6V1B2-Antibody-Polyclonal/PA5-52518>)
- 5) ATP6V0D1/P39 (Cited in 18 publications: <https://www.abcam.com/atp6v0d1p39-antibody-2g12-ab56441.html>)
- 6) ATP6V1H (Citations not listed; validation provided on website: <https://www.fishersci.com/shop/products/v-atpase-h-rabbit-anti-human-polyclonal-thermo-scientific-pierce/PIPA554793>)
- 7) ATP6V1A (Cited in 2 publications including 1 in Nature: [http://www.abnova.com/products/products\\_detail.asp?catalog\\_id=H00000523-M02](http://www.abnova.com/products/products_detail.asp?catalog_id=H00000523-M02))
- 8) RAS (Cited in 106 publications: <https://www.cellsignal.com/products/primary-antibodies/ras-antibody/3965>)
- 9) EGFR (Cited in 936 publications: <https://www.cellsignal.com/products/primary-antibodies/egf-receptor-d38b1-xp-rabbit-mab/4267>)
- 10) Alexa-Fluor 488 goat anti-mouse (Cited in 5438 publications: [https://www.thermofisher.com/order/genome-database/dataSheetPdf?producttype=antibody&productsubtype=antibody\\_secondary&productId=A-11001&version=122](https://www.thermofisher.com/order/genome-database/dataSheetPdf?producttype=antibody&productsubtype=antibody_secondary&productId=A-11001&version=122))
- 11) Alexa-Fluor 488 goat anti-rabbit (Cited in 6210 publications: <https://www.thermofisher.com/antibody/product/Goat-anti-Rabbit-IgG-H-L-Cross-Adsorbed-Secondary-Antibody-Polyclonal/A-11008>)

## Eukaryotic cell lines

## Policy information about cell lines

## Cell line source(s)

-MEF cell lines were obtained from the National Cancer Institute (NCI).  
 -SW48, SW48 KRASG12D/+, SW48 KRASG12V/+ and SW48 KRASG13D/+ cell lines were obtained from Horizon Discovery.  
 -MDA-MB-231 CRISPRi cells were obtained from Dr. Hani Goodarzi at UCSF. Parental MDA-MB-231 cells were from ATCC.  
 -Cell lines were obtained from ATCC: H1944 (CRL-5907), A427 (HTB-53), A549 (CRM-CCL-185), SW1271 (CRL-2177), H292 (CRL-1848), H358 (CRL-5807), H1299 (CRL-5803), H460 (HTB-177), H1703 (CRL-5889), H2170 (CRL-5928), H2452 (CRL-5946), NCI H82 (HTB-175), Calu-3 (HTB-55), H838 (CRL-5844), H1975 (CRL-5908), H1650 (CRL-5883), H28 (CRL-5820), CFPAC-1 (CRL-1918), Capan-1 (HTB-79), Panc 02-13 (CRL-2554), ASPC1 (CRL-1682), Panc1 (CRL-1469), BxPC3 (CRL-1687), MDA-MB-231 (HTB-26), Sk-Br-3 (HTB-30), MCF7 (HTB-22), MDA-MB-436 (HTB-130), HCT116 (CRL-247EMT), Colo201 (CCL-224), N87 (CRL-5822), RKO (CRL-2577), SW48 (CCL-231), CaCO2 (HTB-37), SkMeI5 (HTB-70), SKMEL30 (HTB-73), A375 (CRL-1619), A2058 (CRL-11147), DUI145 (HTB-81), PC3 (CRL-3471), U251 (HTB-17), U87 (HTB-14), HL-60 (CCL-240), HepG2 (HB-8065).  
 LOX IMVI, MeJuso, BT474 and HCC1937 cells were a gift from the Oritz-Urda lab at UCSF originally sourced from ATCC or as gifts. ES2, OVCAR8, HEYA8, and HEY cells were a gift from the Smith-McCune lab at UCSF originally sourced from ATCC.

## Authentication

-MEF parental cells were validated at the NCI using karyotyping. For the derived MEFs with KRAS mutations, the endogenous KRAS removal was authenticated via PCR to compare to a mouse reference gene Tfrc. MEF cells with subsequent addition of KRAS mutants were exome sequenced and compared with a mouse reference genome at a genomics lab (GRCm38 mm10).  
 -SW48 cells were validated by Horizon Discovery using genotyping (gDNA and cDNA):  
[https://horizondiscovery.com/-/media/Files/Horizon/resources/Data%20Sheets/88/HD%20103-011%2000058\\_DataSheet.pdf](https://horizondiscovery.com/-/media/Files/Horizon/resources/Data%20Sheets/88/HD%20103-011%2000058_DataSheet.pdf)  
[https://horizondiscovery.com/-/media/Files/Horizon/resources/Data%20Sheets/31/HD%20103-007%2000053\\_DataSheet.pdf](https://horizondiscovery.com/-/media/Files/Horizon/resources/Data%20Sheets/31/HD%20103-007%2000053_DataSheet.pdf)  
[https://horizondiscovery.com/-/media/Files/Horizon/resources/Data%20Sheets/70/HD%20103-002%2011917\\_DataSheet.pdf](https://horizondiscovery.com/-/media/Files/Horizon/resources/Data%20Sheets/70/HD%20103-002%2011917_DataSheet.pdf)  
 -MDA-MB-231 CRISPRi cells were validated by Dr. Hani Goodarzi's lab.  
 -A549 cells were validated by ATCC using STR cell authentication services.  
 -Other cells obtained from ATCC relied on the company's certificates of analysis. No other independent authentication was performed.

## Mycoplasma contamination

-MEF cells were tested for mycoplasma at the NCI and tested negative.  
 -Horizon Discovery states that all their cell lines are tested for mycoplasma in their Data Sheets.  
 -Dr. Goodarzi's lab tested for mycoplasma in MDA-MB-231 CRISPRi cells every 4 months.  
 -Our lab uses MycoAlert Detection Kits from Lonza Bioscience. All cell lines were tested for mycoplasma and were found to be negative.

Commonly misidentified lines  
(See [ICLAC](#) register)

No misidentified cell lines that we know were used for this study.

## Animals and other organisms

Policy information about [studies involving animals](#); [ARRIVE guidelines](#) recommended for reporting animal research

Laboratory animals	-For A549 xenografts: 6-8-week old athymic nude female mice (Charles River strain # 088, homozygous NU/NU) -For SW48 xenografts: 6-8-week old athymic nude female mice (Taconic model # NCRNU-F, CrTac:NCR-Foxn1 sp/sp)
Wild animals	The study did not involve wild animals.
Field-collected samples	The study did not involve samples collected from the field.
Ethics oversight	All animal procedures were performed under IACUC approved protocols and guidelines. Mouse manipulations were performed in accordance with UCSF's IACUC protocol AN179973.

Note that full information on the approval of the study protocol must also be provided in the manuscript.

## Flow Cytometry

### Plots

Confirm that:

- The axis labels state the marker and fluorochrome used (e.g. CD4-FITC).
- The axis scales are clearly visible. Include numbers along axes only for bottom left plot of group (a 'group' is an analysis of identical markers).
- All plots are contour plots with outliers or pseudocolor plots.
- A numerical value for number of cells or percentage (with statistics) is provided.

### Methodology

Sample preparation	-For CRISPR re-test experiments, populations of cells containing 20-50% sgRNA-expressing cells were treated with the indicated compounds for the indicated times, dissociated, and immediately run on the flow cytometer without further processing.  -For Apoptosis Assays: MEFs from the NCI or cancer cells obtained from ATCC were treated with 100 nM 249C for 48 hours and following two washes with ice-cold PBS, they were stained using a FITC Annexin V/PI Apoptosis Detection kit (BD Pharmingen) by following the manufacturer's recommendations.
Instrument	BD™ LSR II flow cytometer (Serial# H47100133) - BD Biosciences
Software	FACSDiva software (version 8.0) was used for data acquisition and Excel (2016) was used for data analyses.
Cell population abundance	For Apoptosis Assays: Samples were analyzed by flow cytometry but no cell sorting was performed.
Gating strategy	-For CRISPR re-test experiments, an FSC/SSC gate was applied followed by a BFP gate to demarcate sgRNA-expressing cells.  -For Apoptosis Assays: Preliminary FSC/SSC gates were applied followed by removal of doublets (FSC-H vs FSC-A and also SSC-H vs SSC-A). Next single color controls (FITC only or PI only) and double positive controls (FITC+ & PI+) were run to set gates for the double positive population. Finally, untreated and 249C-treated samples were run keeping these gates constant for all.

- Tick this box to confirm that a figure exemplifying the gating strategy is provided in the Supplementary Information.